SEMARAK ILMU PUBLISHING

Journal of Advanced Research in Fluid Mechanics and Thermal Sciences

Journal homepage:
https://semarakilmu.com.my/journals/index.php/fluid_mechanics_thermal_sciences/index
ISSN: 2289-7879

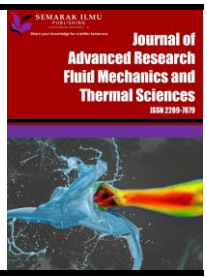

Experimental Investigation of Low Reynolds Number Flow Around a Serrated NACA 0015 Airfoil

Mohamed Ibren[1], Amelda Dianne Andan[1,*], Waqar Asrar[1], Mohammed Abdulmalek Mohammed Aldheeb[1], Mohd Rashdan Saad[2]

[1] Department of Mechanical Engineering, Faculty of Engineering, International Islamic University Malaysia, 53100, Kuala Lumpur, Malaysia
[2] Department of Aeronautics Engineering and Aviation, National Defence University of Malaysia, Kuala Lumpur, 57000, Malaysia

ARTICLE INFO

Article history:
Received 20 September 2023
Received in revised form 30 November 2023
Accepted 14 December 2023
Available online 31 December 2023

Keywords:
Low-Reynolds number; NACA0015 airfoil; aerodynamics; serration; comb; porous

ABSTRACT

The study of low Reynolds number flows has triggered the interest of many researchers. This concern is attributed to the presence of various vortex structures that significantly affect aerodynamic performance. The study of such phenomena offers an opportunity to better understand and predict the behavior of fluid flows in three dimensions, leading to improved design strategies for aerodynamic systems. This study intends to examine the performance of different NACA 0015 airfoil configurations namely, baseline, serration, comb, comb-serration and poro-serrated, emphasizing on their influence on aerodynamic characteristics and flow structure. Experimental work is performed to provide valuable insights into the behavior of the flow field and the underlying physical phenomena. The current study has shown that the mean streamwise velocity of the serrated, combed, and comb-serrated configurations exhibit more stable flow patterns compared to the baseline airfoil. These patterns suggest a promising approach for delaying flow separation. In contrast, the poro-serrated model exhibited a more disordered flow pattern. Remarkably, when subjected to a 10-degree angle of attack, all the modified trailing-edge designs showcased minimal separation zones compared to the baseline configuration. At the same angle, the baseline's shear layer disintegrates, while the poro-serrated model displays increasing disturbance and separation. Conversely, the comb-serrated and serration models exhibit a smaller increase in unsteadiness. Furthermore, the study indicated that Musou black paint exhibits a higher rate of light absorption compared to flat black paint, but it demonstrates higher reflection levels on a poro-serrated surface. Collectively, the outcomes of this investigation hold significant implications for enhancing aerodynamic system designs.

1. Introduction

Investigating low Reynolds number flows offers an opportunity to gain deeper insights into the fundamental principles of aerodynamics, particularly in relation to the behavior of fluids around airfoils and wings operating in this regime. Recent experimental studies on low Reynolds number flows have shown great improvement due to the technological advancement in experimental

* *Corresponding author.*
E-mail address: ameldadianne@iium.edu.my

https://doi.org/10.37934/arfmts.112.2.137160

techniques. Consequently, this has sparked interest in comprehending the intricate characteristics of low Reynolds number flows.

This flow regime is three-dimensional and very complex due to various forms of vortical phenomena. The flow structures around an airfoil are entirely different for a wide range of Reynolds numbers. Flow separation and formation of laminar separation bubbles (LSB) are among the main features found in this regime [1]. The flow separates due to a strong adverse pressure gradient [2,3]. Moreover, stronger adverse pressure gradients and weaker fluid momentum would keep the flow separated, hence forming a considerable wake region downstream of the trailing edge [4]. Likewise, the separated flow field may interfere with the laminar boundary layer (LBL) and begin to form unstable shear layers known as hydrodynamic instabilities. These shear layers disintegrate inconsistently into a chaotic flow due to the changes in the fluid pressure and velocity [5,6]. On the other hand, the separated flow might go through a transition to turbulence and thus the turbulent boundary layer (TBL) is formed in the wake of a vortical structure known as reverse flow [3,5]. This trend is because of an increase in the fluid momentum after the transition. As a result, the accelerated shear layers reattach to the airfoil surfaces to develop a region of low velocity and low pressure known as a laminar separation bubble [3,5,7]. Besides that, the laminar separation bubble might separate or reattach again after the trailing edge [4].

The laminar separation bubble is often categorized into long and short bubbles [8]. This classification was based on the length scales of displacement thickness at the separation point and the chord length. Long bubbles affect pressure fluctuations, whereas short bubbles can alter the potential flow over the airfoil surface [3]. Additionally, the size of the bubble formed depends on the Reynolds number of the flow, the bubble might form, burst or vanish due to a slight change in the Reynolds number [9,10]. For instance, short bubbles at times burst to form a huge bubble that either reattaches with the surface or flows towards the wake without reattachment. Bursting of the bubbles control the stalling of the airfoil [3]. The features of the bubbles do not depend on Reynolds number only but also on the angle of attack (AoA) [11]. At smaller angles of attack (below stall angle), the bubbles determine the transition behavior of the flow. The bubbles are formed on both sides of the airfoil for small angles of attack. When the angle of attack is increased, the size and the length of the laminar separation bubble decreases gradually. Concurrently, the bubbles rapidly shift towards the leading edge on the airfoil suction side [12], whereas the boundary layer moves closer to the trailing edge on the pressure side [13]. Moreover, airfoil geometry and turbulence intensity affect the wake features, for example, the vortex size, rotational direction, and shedding frequency [14,15]. Some studies have demonstrated the dependence of aerodynamic performance and radiated noise over 2D airfoils towards flow conditions at relatively low-Reynolds numbers [4,16]. A slight change in the airfoil profile would alter the lift coefficient, separation features and stalling behavior [17]. Similarly, separation location and stalling characteristics affect aircraft structure and aerodynamic performance [18]. This has sparked interest among researchers in developing effective control tools capable of mitigating noise without affecting aerodynamic performance.

In recent years, the application of a modified trailing edge such as serrated, has been demonstrated experimentally and numerically [3,19-25]. However, in most cases, these serrations are made into a thin flat plate and inserted into the main body of the airfoil [26]. Theoretically, the geometry of the serration destructs the coherent structure between the acoustic waves [27,28]. On the contrary, in an experimental work examining the wall pressure power spectral density and the coherent structure along the serration edges shows that the flow field is almost identical [29]. Nevertheless, they have also observed vortices along the serration edges thus affecting the momentum and turbulence energy distribution [29]. Based on other studies, serration affects the flow-field structure, in reducing the amplitude of the unsteady pressure fluctuations along the span

hence at times it is referred to as the source cut-off effect [30-32]. Currently, little study has successfully incorporated a trailing edge design that accurately matches the real-world geometry of the models. Additionally, it is advisable to contemplate and seamlessly integrate this approach into the new designs, given the significant influence the trailing edge's profile wields over the flow structure.

Another exceptional technique that is incorporated with serration design is poro-serrated. This approach offers further reduction in vortex shedding [33]. Moreover, metal foams and porous coatings covering a circular cylinder have shown notable noise reduction due to the stability of the vortical and turbulence structure near the wake [34,35]. The most frequently used parameters to describe porous materials are porosity, airflow resistivity and tortuosity [36,37]. Porosity can be defined as the measure of the void space in a material whereas resistivity indicates the ability of a material to oppose the flow through its void spaces [1]. The porous material should be permeable to the normal component velocity at the source and impermeable to the average flow velocity. This reduces unwanted flow leakage and thus maintains aerodynamic performance [36]. Over and above that, the porosity should progressively increase downstream of the porous material. However, this cannot be achieved with cutting insertions due to the introduction of surface discontinuity [36].

Some recent studies have confirmed that a porous trailing-edge has the potential of reducing breakdown of spanwise pressure fluctuations and a decrease in streamwise convection velocity [38-40]. Furthermore, porous treatment has demonstrated the capability to stabilize turbulence structures, reducing vortex shedding, and control flow-induced instabilities such as pressure distributions and fluctuations [38,41-43]. For instance, some of the concepts that can be applied to reduce vortex shedding are the utilization of smaller pore size with a sub-millimeter diameter as well as correct placement of the porous region on the airfoil's surface, which will reduce pressure fluctuation and peak swirl velocity [43].

The vortices in 3D flows are complex due to interactions of multiple physical processes, requiring advanced techniques like Particle Image Velocimetry (PIV) to study flow structure. 2D Particle Image Velocimetry (2D-PIV), also known as planar PIV, uses one camera, a dual-cavity pulsed laser light source, light-sheet optics, and a synchronizing unit. Tracer particles are added to the flow and illuminated in the measurement plane. Velocity is calculated from the particle displacement of the two images taken within a very short time. To mitigate surface reflection, one can either paint the area where the laser sheet hits, use a transparent material, or apply fluorescent paint. However, fluorescent paint may obscure some flow details. Covering objects near the PIV camera field of view is also essential. The light sheet must be aligned perpendicular to the flow and camera coordinate system to minimize errors; this can be achieved by calibrating sheet alignment and thickness. Additionally, accurate results require a well-focused, high-contrast image with good exposure, which can be enhanced by setting a large aperture and increasing the aperture f-number afterwards. This procedure increases the depth of field and improves focus by reducing the amount of light captured by the camera. On the other hand, factors such as particle polydispersity, particle distribution, concentration, and perturbations can affect tracer performance and the accuracy of results. A technique to improve accuracy is to have at least 10 particles per interrogation window. In this experiment, diligent efforts were made to address most of these factors, thus ensuring the result's accuracy.

The current study describes the development and the effects of various passive methods on the fluid flow around a 2-D NACA 0015 airfoil placed at various angles of attack ($0^0 < \alpha > 10^0$) to a flow at a chord-based Reynolds number of 1.6 x 10^5. The findings of this study hold significant implications for the field of aerodynamics, particularly in relation to the performance of airfoils and wings operating in the low Reynolds number regime. To further assess the influence of different serration

designs on the flow parameters, combed, poro-serrated and comb-serrated trailing-edge were included in the experimental analysis. In this current work, streamwise velocity components, velocity profile along the airfoil's top surface and vortical structures are investigated and presented.

2. Methodology

2.1 Experimental Set-up

For This study implemented a Particle Image Velocimetry (PIV) technique to evaluate the velocity field in an open-circuit wind tunnel system. The present study focuses on the flow structure analysis of a NACA 0015 airfoil with chord length 0.15 m and span length of 0.298m, as depicted in Figure 1. In addition to the baseline NACA 0015 airfoil, the study also examines other trailing edge configurations, including serrated, comb, comb-serrated, and poro-serrated, as displayed in Figure 2. The experimental setup consisted of a test section with dimensions of 300 mm x 300 mm. The flow conditions in the tunnel were set to have a mean velocity of 15.78 m/s and a Reynolds number of approximately 1.6 x 10^5. The experiments were conducted at a range of angles of attack, varying from 0 to 10 degrees, with the incidence angles set manually using a protractor that had a resolution of 1 degree. The upstream portion of the flow includes a contraction section equipped with honeycomb-like screens, effectively reducing the turbulence intensity to approximately 0.04% as determined by the fan's frequency response of 10 Hz. The maximum solid blockage was evaluated and found to be around 7.4%. Consequently, no adjustments for blockage were made to the recorded data, given that this value is close to the acceptable threshold [44,45].

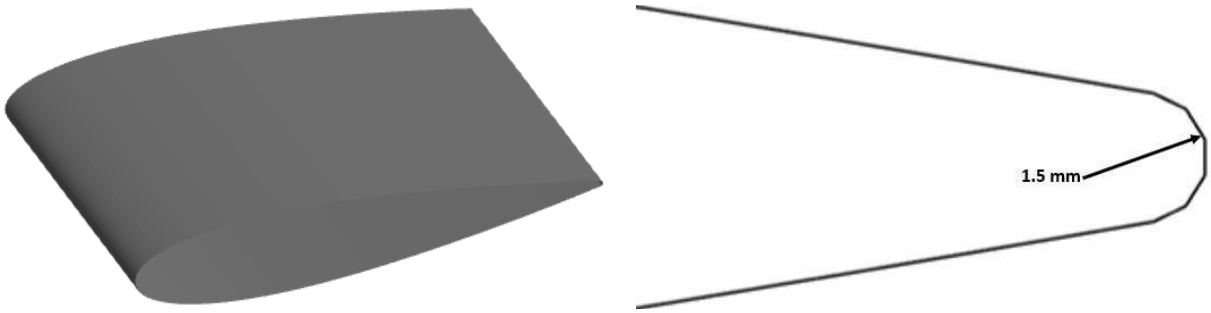

Fig. 1. Geometry of NACA0015 airfoil used in this study

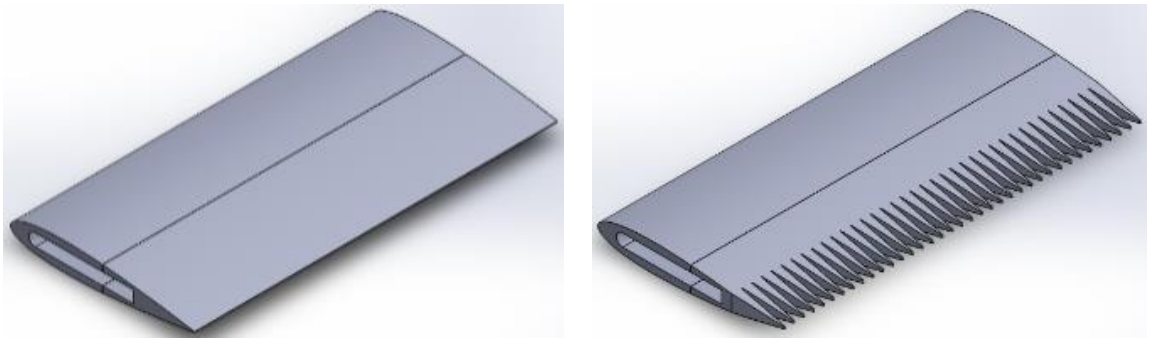

(a) Baseline Model (b) Serrated TE Model

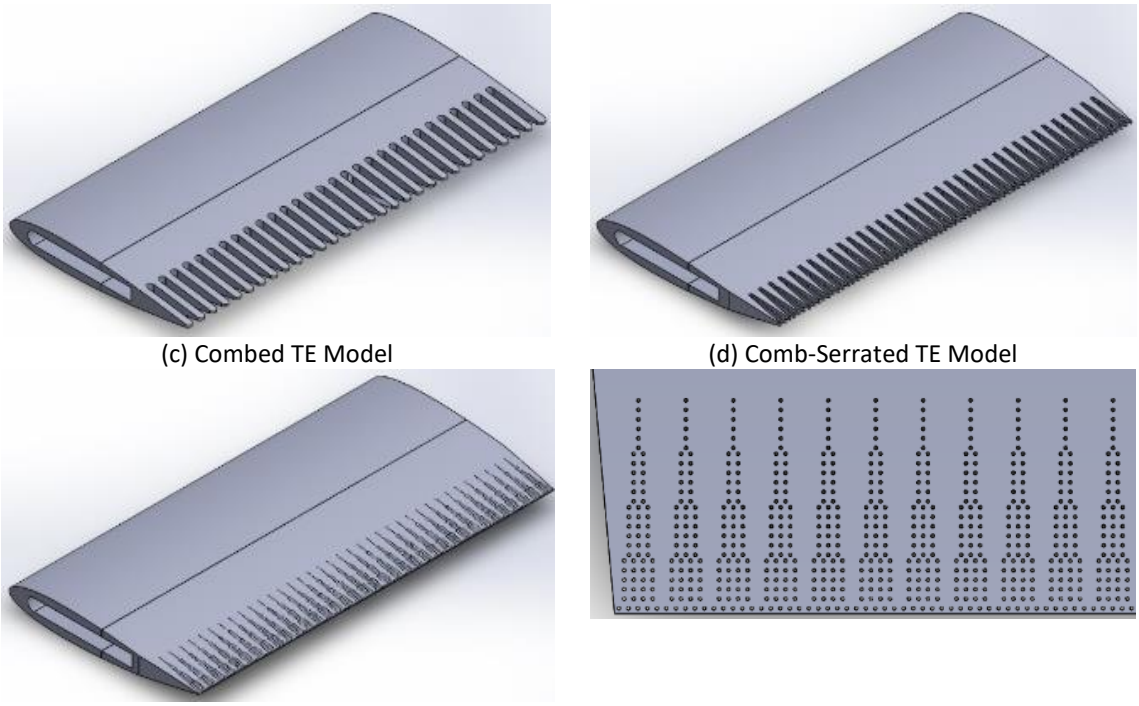

(c) Combed TE Model (d) Comb-Serrated TE Model

(e) Poro-Serrated TE Model (f) Close-Up View of Poro-Serrated TE

Fig. 2. Geometry of all the trailing-edge sections used in this study

The 2D Particle Image Velocimetry (PIV) system was performed in a plane perpendicular to the flow direction using the configurations depicted in Figure 3. To improve particle visibility, the flow was seeded with Di-ethyl-hexyl-sebacate (DEHS) particles with an average diameter of 1 µm. The seeding is employed since it has low vapour pressure, is non-toxic and easily dispersible in the flow due to its low density. The seeding material was illuminated by a laser sheet produced by a dual-pulsed Nd:YAG laser with a pulse energy of 200 MJ, frequency of 15 Hz, and wavelength of 532 nm. The laser beam was introduced into the test section through the top wall and conditioned into a thin sheet with an estimated thickness of 1 millimeter. The laser was calibrated by utilizing two rulers at both ends of the laser sheet to ensure perpendicularity of the laser sheet in the flow direction as shown in Figure 3.

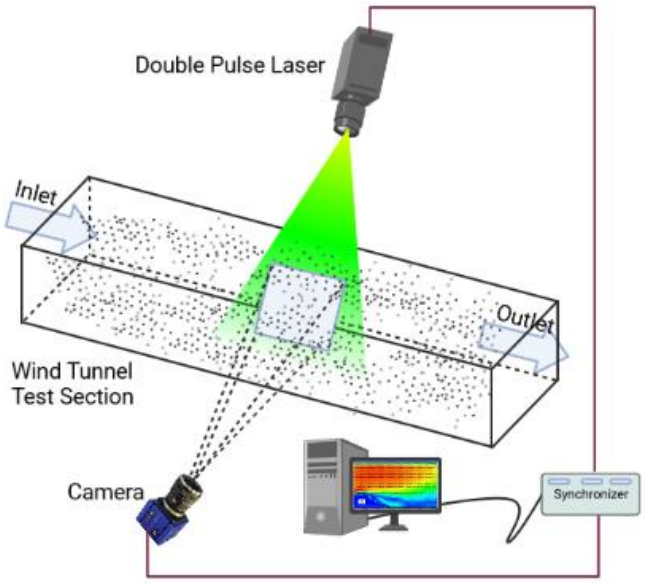

Fig. 3. Schematic of PIV setup in the wind tunnel

Furthermore, the particle image velocity (PIV) data was recorded by a high-speed camera equipped with a 50 mm lens and a resolution of 2752 x 2200 pixels. The camera was synchronized with the laser pulses through a programmable timing unit (PTU) utilizing DaVis 10.0 software. The camera was calibrated with a standard calibration target to determine its intrinsic parameters such as vertical and horizontal orientation with respect to the field of view. The field of view was carefully chosen to provide a clear and comprehensive view of both the upstream and downstream flow regions. This was achieved by ensuring that the field of view was appropriately sized to capture all relevant flow information, providing a comprehensive understanding of the flow dynamics in the test section. The flow field was calibrated using tracer particles. In addition, the images were acquired using a dual-frame PIV approach with a sampling rate of 12.95 Hz, and an exposure time of 50 µs per frame. Moreover, the camera used in the experiment was originally set to have a relative aperture setting of f/1.8. This parameter was used to concentrate the particles in the flow field effectively. However, to improve the focus of the acquired images, the aperture was later increased to f/2.8, which reduced the quantity of light and provided sharper images.

A substantial number of 500 images were recorded and processed using a cross-correlation algorithm. The final interrogation window size was 32 by 32 pixels with 75% image overlap, with each window having 10 particles on average. The Particle Image Velocimetry (PIV) measurements were captured three times and averaged to enhance accuracy and reliability, mitigating the impact of random errors and transient flow variations. The particle displacements and time-difference between the two frames were used to calculate the velocity field, which was then statistically analyzed and visualized using vector plots and contour plots. The accuracy of the results was limited by factors such as the reflection from the surface, particle image resolution, laser light intensity, camera exposure time, and the presence of flow structures such as vortices and wakes. Moreover, to enhance the experiment's precision and minimize the impact of surface reflection on the results, a novel paint called Musou black, which has not been previously employed in any PIV analysis, was utilized. This paint has been carefully selected based on its optical properties and ability to reduce surface reflection, thereby improving the accuracy of the experiment. The measurements were repeated multiple times to ensure the quality of the results. Table 1 summarizes the parameters for the PIV experiments.

Table 1
Parameters used in 2D Particle Image Velocimetry (PIV) measurements

Parameters	Units	Symbols	Data
Focal Length	mm		50
Aperture Number		f/	2.8
Field of View	mm^2	FoV	160 x 160
Imaging Resolution	pixels	S	2752 x 2200
Interrogation Window	pixels		32 by 32
Sampling Frequency	Hz	f_s	12.95
PIV Frame Mode			Double frame mode
Exposure Time	µs	Δt	50
Freestream Displacement	pixels	Δx	10

3. Effects of Musou Black Paint

Musou Black paint is created from ultra-fine carbon particles known as nitrogen-doped graphene, which equips it with a deep and robust black colour. This paint has the potential to absorb virtually all the light that strikes its surface, leaving it an incredibly dark substance. The absorption rate of Musou Black paint is believed to be close to 99.965%, yielding unusually low reflectivity [46]. As a

result, it is suited for usage in optical applications such as experiments on Particle Image Velocimetry (PIV). Given the aforementioned qualities and considering the absence of prior research employing Musou Black paint in PIV measurement, this study intends to compare it with the conventional Flat black paint. The two types of paint differ significantly in terms of their light absorption capabilities. Flat black paint has an absorption rate of close to 80%. Given these numbers, it is evident that Musou Black has a more significant light absorption capability than Flat Black paint. The results provided in Figure 4 demonstrate that Musou Black paint surpasses Flat Black paint in the baseline, serration, and comb models when it comes to light reflection from the surface. Specifically, Musou Black demonstrated reduced reflection of light from these models when compared to Flat Black. However, the situation is flipped with the poro-serrated type, where flat black exhibits less reflection. The variation in light reflection between the two paints is likely related to the existence of holes in the poro-serrated model. The perforations may make the light scatter differently, resulting in a distinct reflection pattern. Additionally, the unique pigments employed in the composition of Musou Black paint may contribute to the disparity in reflection. These pigments may influence how the paint interacts with light, resulting in differences in reflection between the two types of paint. Therefore, Musou black paint is the recommended option for all the other models, such as the baseline, serration, comb, and comb-serrated models. As a result, it is commonly used to paint these models, whereas the poro-serrated model is painted with flat black paint.

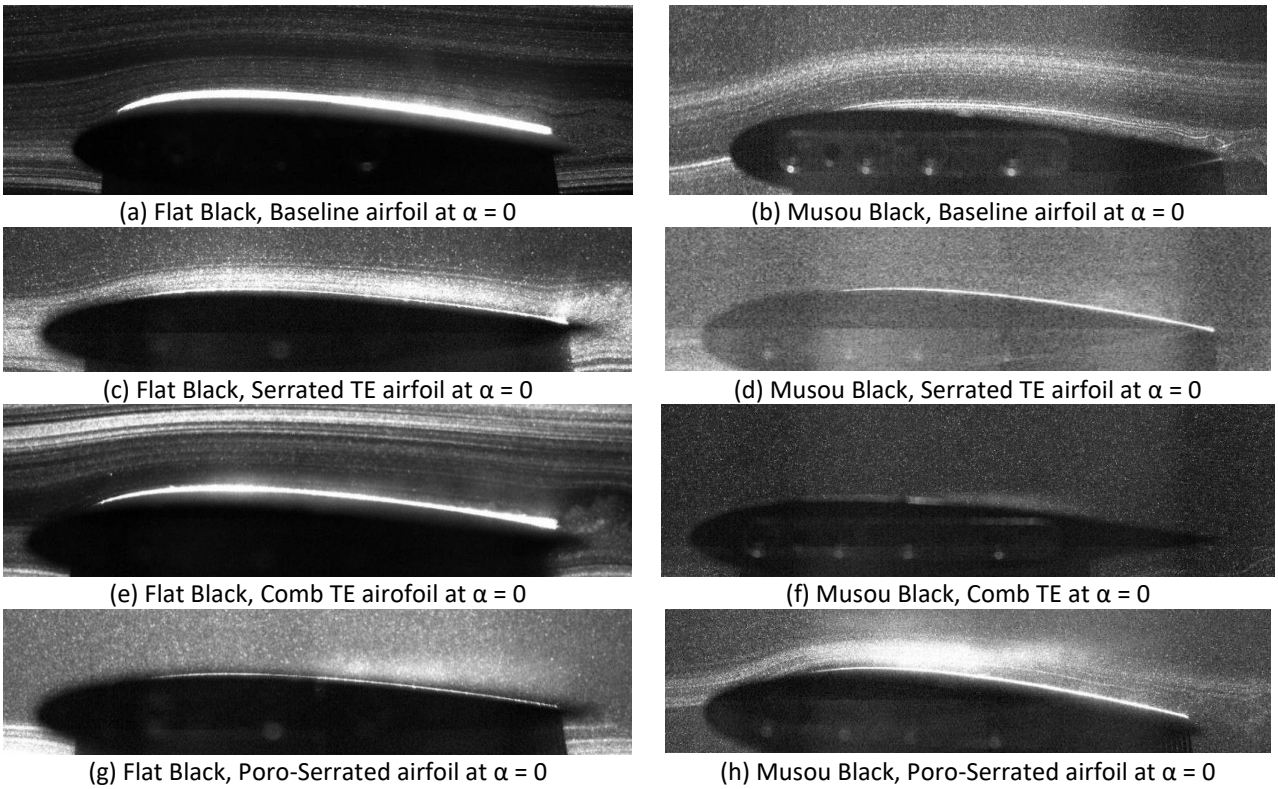

(a) Flat Black, Baseline airfoil at α = 0
(b) Musou Black, Baseline airfoil at α = 0
(c) Flat Black, Serrated TE airfoil at α = 0
(d) Musou Black, Serrated TE airfoil at α = 0
(e) Flat Black, Comb TE airofoil at α = 0
(f) Musou Black, Comb TE at α = 0
(g) Flat Black, Poro-Serrated airfoil at α = 0
(h) Musou Black, Poro-Serrated airfoil at α = 0

Fig. 4. Surface reflection from Musou and Flat black painted surface at α = 0^0

4. Experimental Results

4.1 Streamwise Velocity Field

Velocity contour scale, ranging from -1.5 to 1.2 as depicted by Figure 5 to Figure 10, quantifies the local velocity's relationship to the free stream velocity in a fluid flow field, providing insights into deceleration, acceleration, and stagnation zones within the flow. At a zero angle of attack, as represented in Figure 5, the flow over the baseline model is defined by its symmetry and uniformity, without any visible perturbations. The velocity of the flow rises as one goes away from the leading edge, with the maximum velocity measured towards the mid-chord position of the airfoil. This velocity steadily decreases towards the trailing edge. As the angle of attack increases, the flow over the airfoil gets progressively disturbed, resulting in variations in the x-velocity contour as seen in Figure 6 to Figure 10. For example, at an angle of attack of 6 degrees, the flow is observed to first separate from the airfoil's surface, forming a laminar separation bubble. This bubble continues to move upstream as the angle of attack increases to 10 degrees, and its size grows with the rising angle of attack.

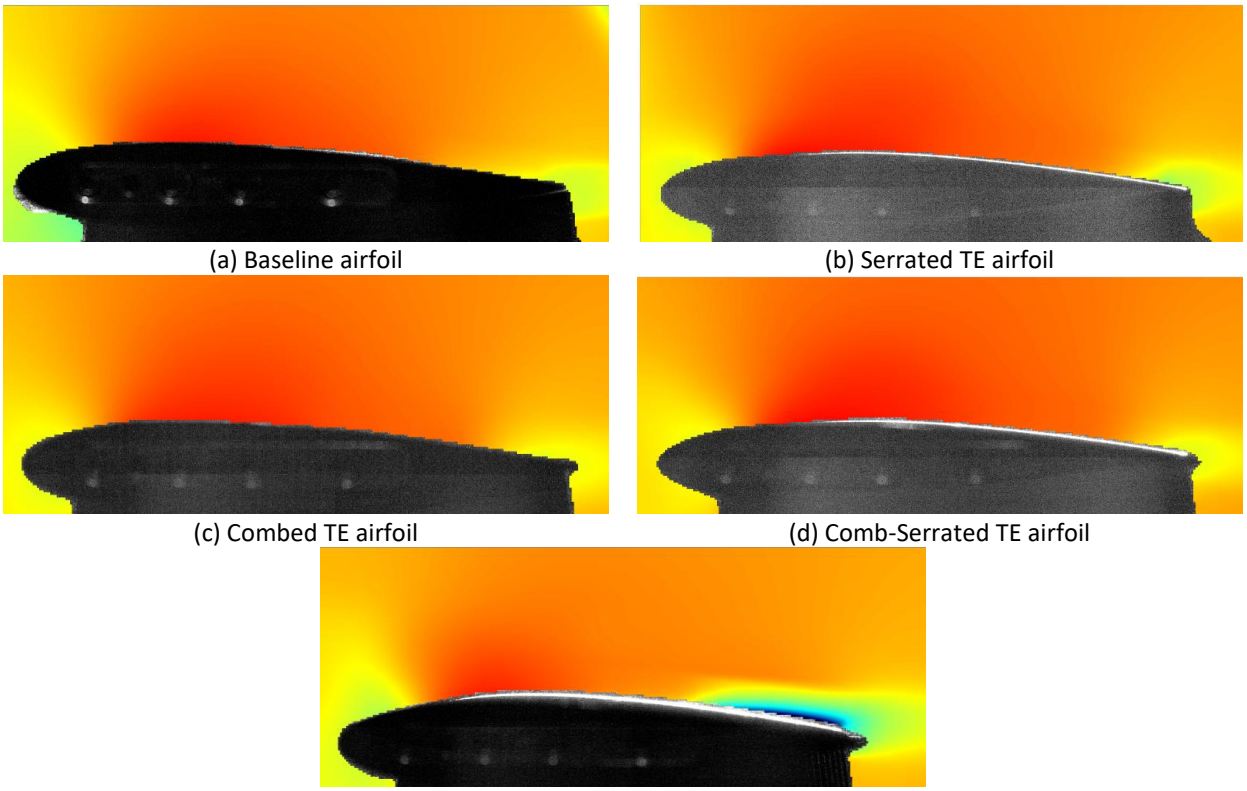

(a) Baseline airfoil (b) Serrated TE airfoil

(c) Combed TE airfoil (d) Comb-Serrated TE airfoil

(e) Poro-Serrated TE airfoil

Fig. 5. Streamwise velocity component at $\alpha = 0^0$

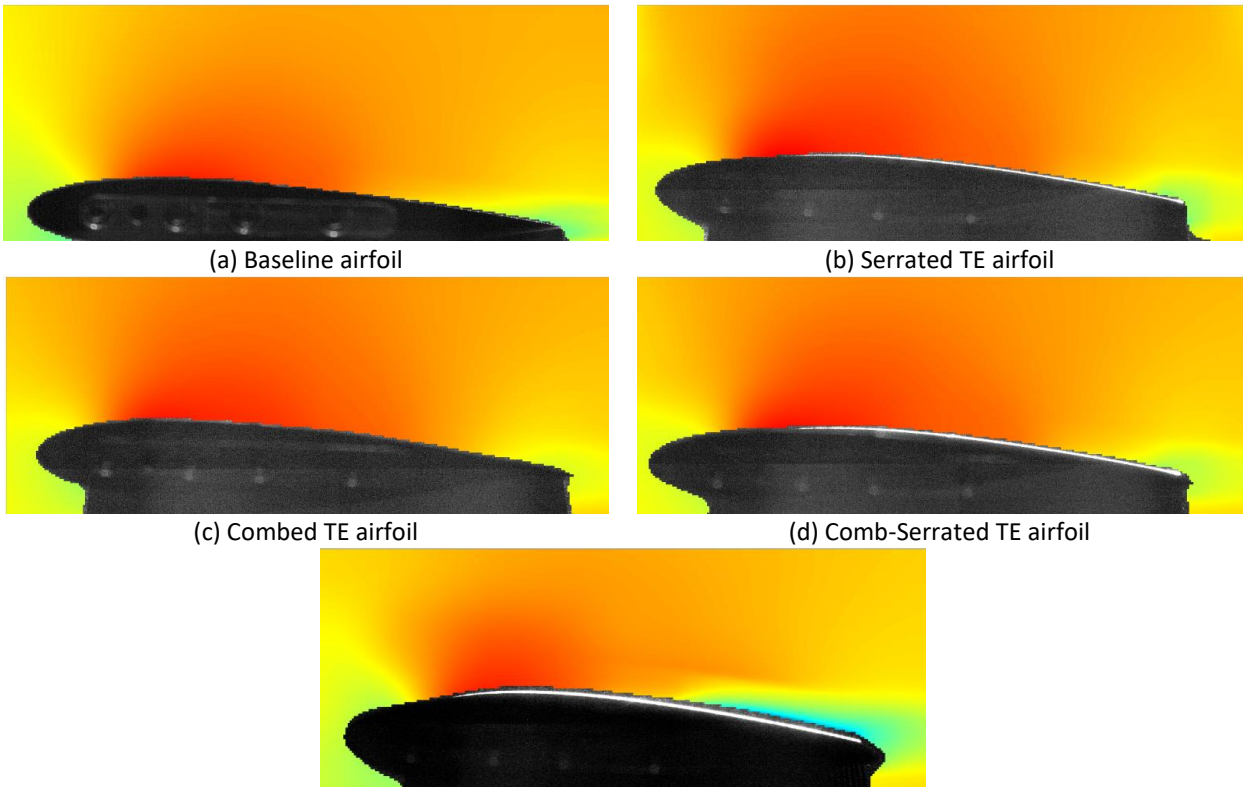

(a) Baseline airfoil (b) Serrated TE airfoil

(c) Combed TE airfoil (d) Comb-Serrated TE airfoil

(e) Poro-Serrated TE airfoil

Fig. 6. Streamwise velocity component at $\alpha = 2^0$

The x-velocity contour of the serrated, combed and comb-serrated trailing edge model demonstrates distinct behaviour compared to the baseline configuration. The flow remains attached to the airfoil's surface until an angle of attack of 8 degrees, where a tiny separation bubble is formed. As the angle of attack increases to 10 degrees, the size of the separation bubble grows. This flow pattern can be due to sawtooth on the trailing edge, which increases the momentum of the flow and enhances its stability as it passes over the trailing edge. The separation bubble is observed to move upstream when the angle of attack increases to 10 degrees. Furthermore, the comb-like structure on the airfoil's trailing edge aligns the flow and decreases the disturbances caused by the discontinuity present in the baseline design. This results in a steadier flow pattern and a reduction in the size of the separation bubble. By synergistically combining the effects of comb and serration, this study reveals that the comb-serrated configuration yields a reduced separation bubble and a notably more stable flow pattern compared to the alternative models. Therefore, serrated, combed, and comb-serrated trailing-edges consistently exhibited stable flow patterns across the entire angles of attack. Moreover, these findings imply that these modified trailing edges design has the potential to effectively delay flow separation.

On the other hand, a poro-serrated trailing-edge model exhibits a radically different flow pattern than the previous airfoil designs. Unlike the other models, this airfoil type shows a laminar separation bubble at a zero angle of attack, a phenomenon not observed in other airfoil forms. This phenomenon may be linked to the porous nature of the airfoil's surface, which enables air to pass through both sides, disturbing the flow and separating the flow. At an angle of attack of 2 degrees, however, no separating bubble is detected, a phenomenon that is not well understood. Furthermore, when the angle of attack increases from 6 degrees, a smaller separating bubble is formed. As the angle of attack progressively increases from 6 degrees to 8 and 10 degrees, the laminar separation bubble demonstrates a noticeable growth in size while also extending further upstream. In general, the flow

pattern of the poro-serrated model appears more turbulent compared to the other modified models, as indicated by the contour of x-velocity. Moreover, when subjected to high angles of attack, these observations suggest that poro-serration has the potential to effectively delay flow separation. Studying the x-velocity contour across various configurations gives essential insights into the flow and separation behaviour over the airfoil's surface, which can guide the design of more efficient and sophisticated wings in the future.

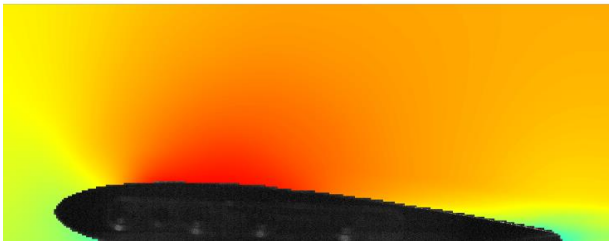

(a) Baseline airfoil

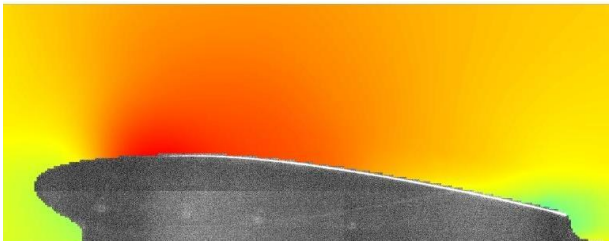

(b) Serrated TE airfoil

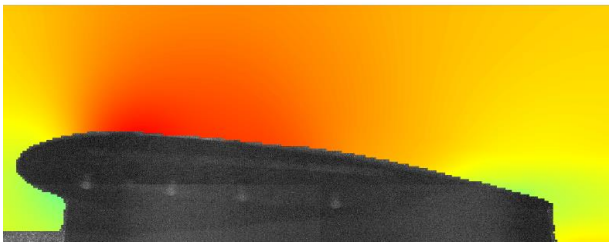

(c) Combed TE airfoil

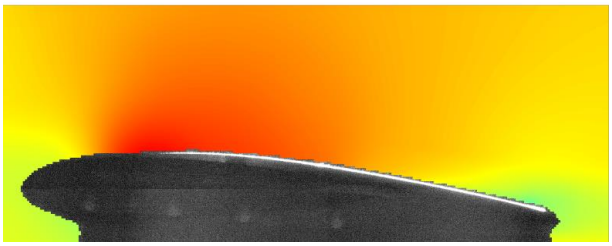

(d) Comb-Serrated TE airfoil

Fig. 7. Streamwise velocity component at $\alpha = 3^0$

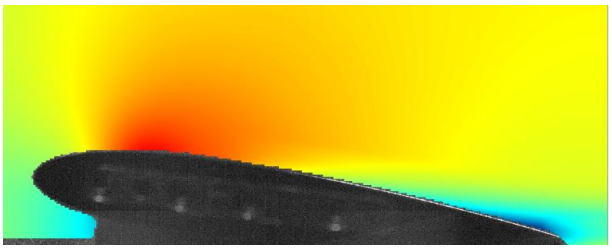

(a) Baseline airfoil

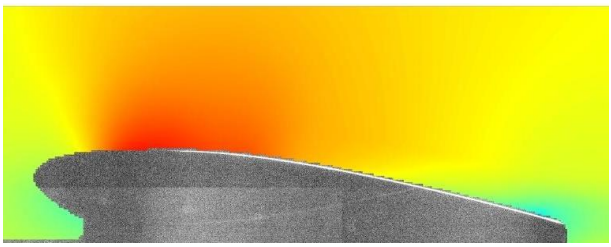

(b) Serrated TE airfoil

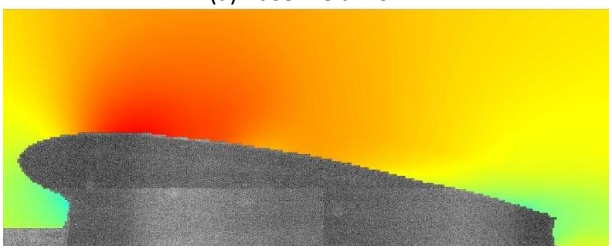

(c) Combed TE airfoil

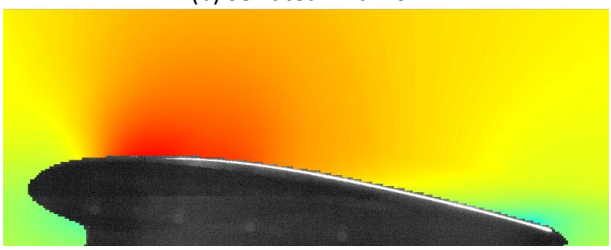

(d) Comb-Serrated TE airfoil

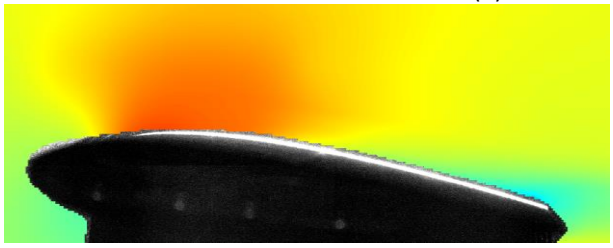

(e) Poro-Serrated TE airfoil

Fig. 8. Streamwise velocity component at $\alpha = 6^0$

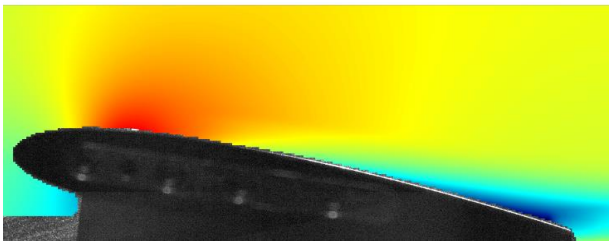

(a) Baseline airfoil

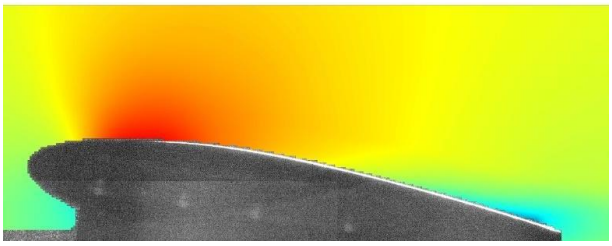

(b) Serrated TE airfoil

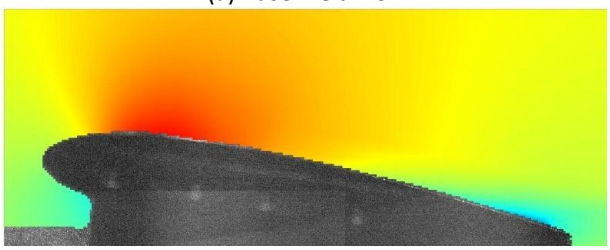

(c) Combed TE airfoil

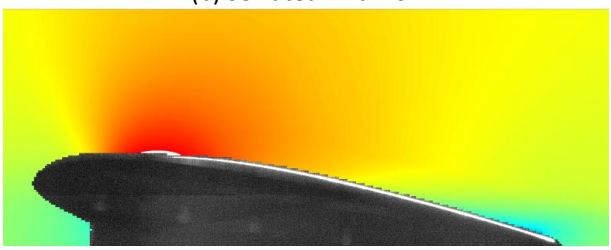

(d) Comb-Serrated TE airfoil

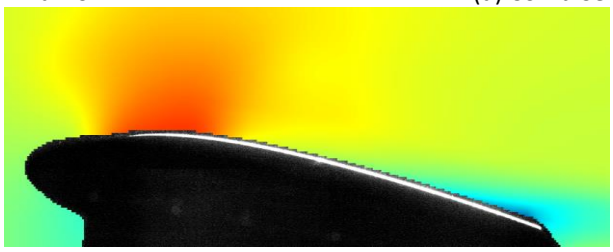

(e) Poro-Serrated TE airfoil

Fig. 9. Streamwise velocity component at $\alpha = 8^0$

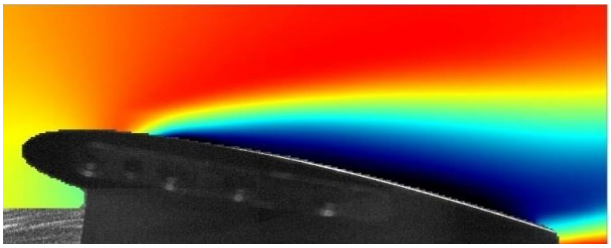

(a) Baseline airfoil

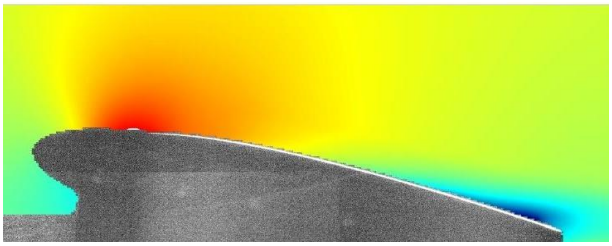

(b) Serrated TE airfoil

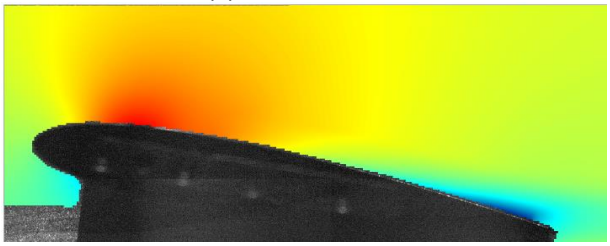

(c) Combed TE airfoil

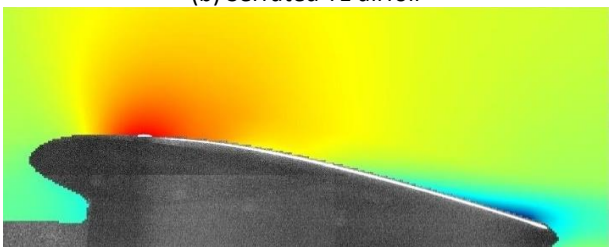

(d) Comb-Serrated TE airfoil

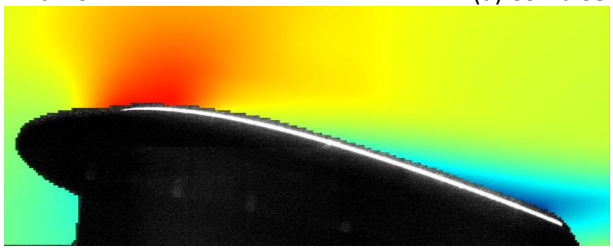

(e) Poro-Serrated TE airfoil

Fig. 10. Streamwise velocity component at $\alpha = 10^0$

4.2 Flow Velocity Distribution

The experimental measurements of the x-velocity profile graphs of several designs, including serrated, comb, comb-serrated, and poro-serrated, are provided in Figure 11 to Figure 16. These graphs offer a detailed explanation of the influence of modified trailing edges on the velocity distribution over airfoil's top surface at various angles of attack. The baseline model displays a smooth and uniform flow at a zero angle of attack, as demonstrated by the slope of the figure. This feature maintains across the spectrum of angles of attack till 6 degrees. However, at an angle of attack of 6 degrees, the velocity profile encounters a sharper gradient and a reversed flow towards the trailing edge. The velocity profile graph's negative gradient shows a reversed flow. This separation area eventually advances upstream of the flow and reaches roughly 0.3c at an angle of attack of 10 degrees. The graphs indicate that the serration model has considerably smoother flow until the angle of attack of 6 degrees, where the flow becomes erratic. However, at approximately 8 degrees, the flow becomes unpredictable and separates from the surface at roughly 0.9c. At an angle of attack of 10 degrees, the separation area is found to have moved to around 0.8c. The size of the separation zone is less than 20% of the chord length, which is lower than the baseline model, where the size of the separation region is around 70% of the chord length at 10 degrees. These findings provide valuable insights into the flow dynamics of the serrated model, highlighting the effective design's ability to minimize the separation area by strategically delaying the separation point, as previously mentioned.

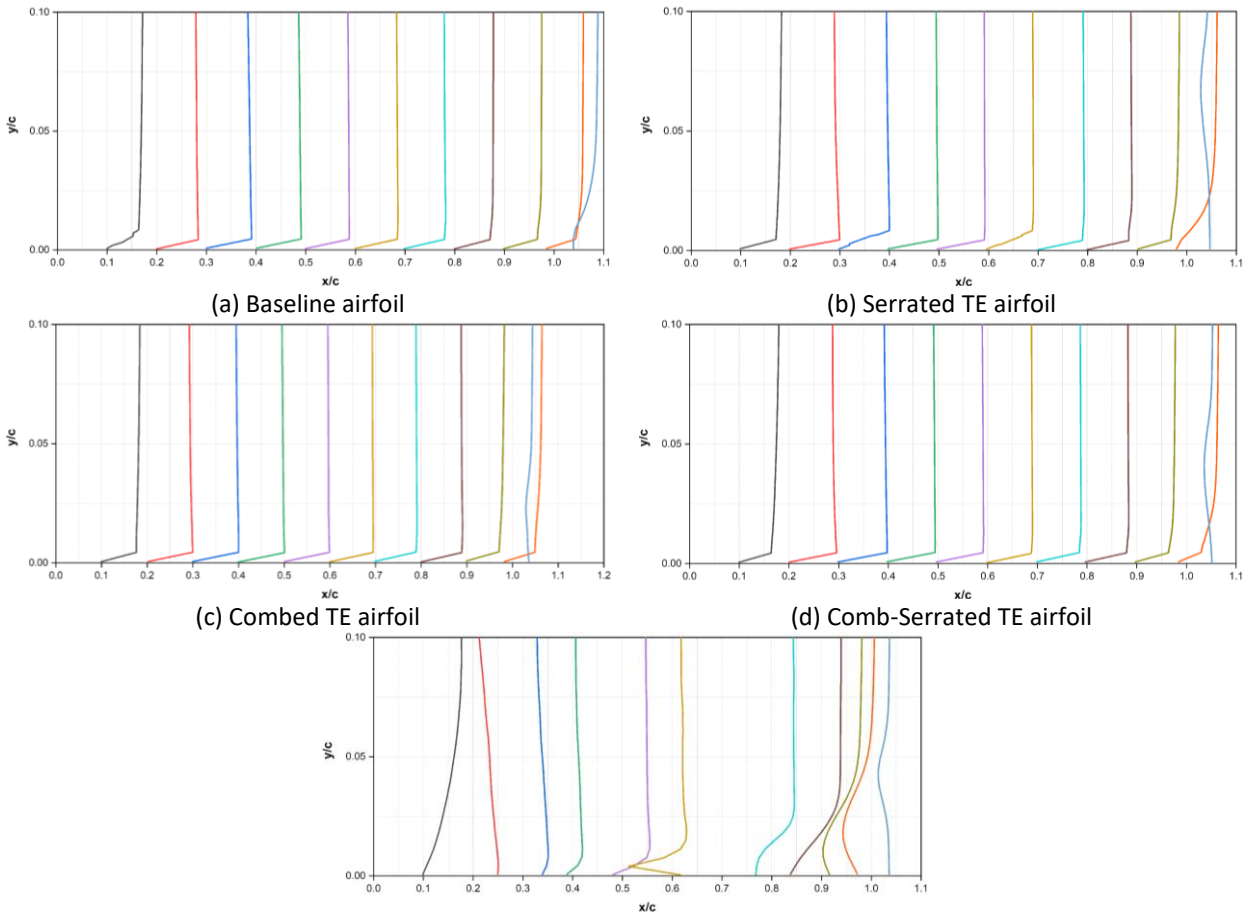

(a) Baseline airfoil

(b) Serrated TE airfoil

(c) Combed TE airfoil

(d) Comb-Serrated TE airfoil

(e) Poro-Serrated TE airfoil

Fig. 11. Velocity Profile at α = 0^0

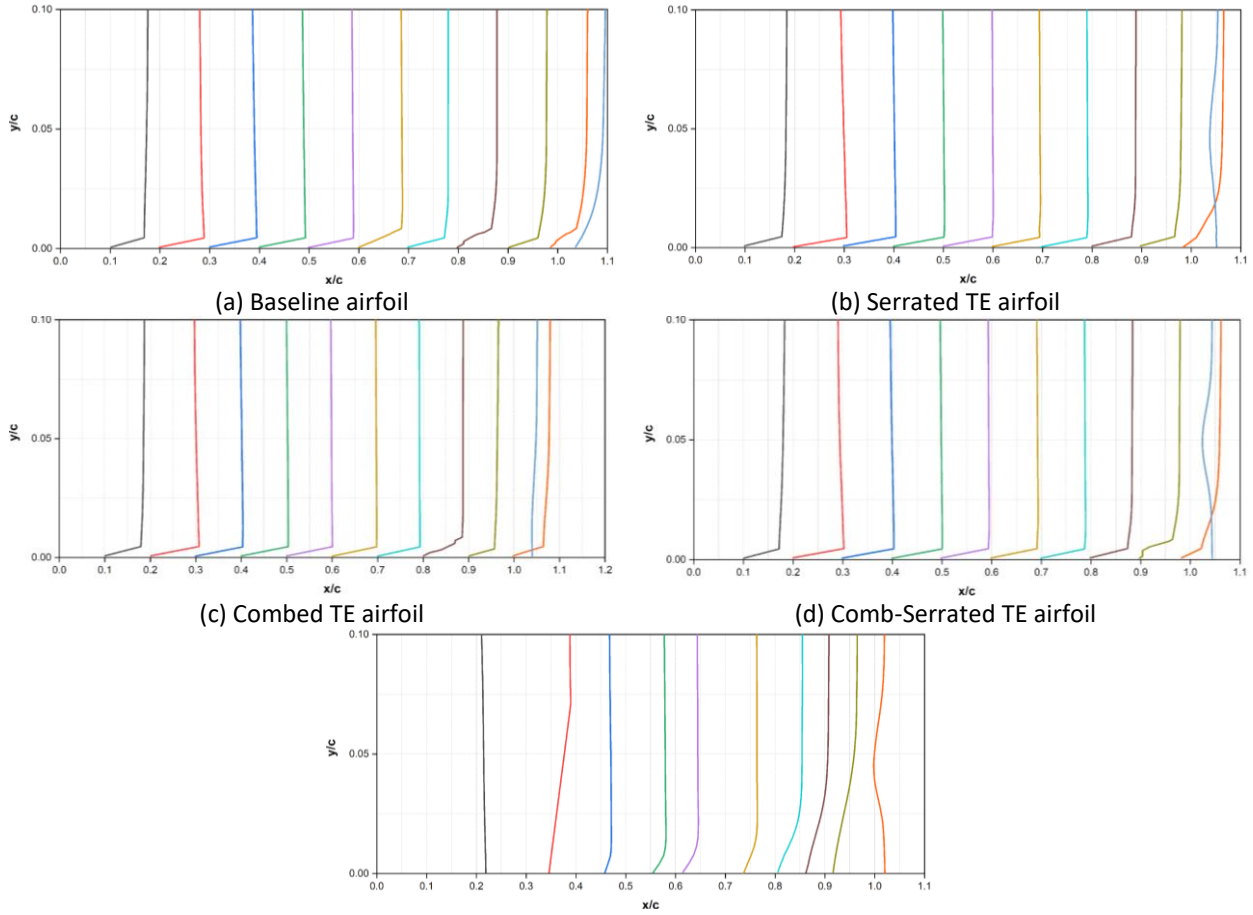

(a) Baseline airfoil (b) Serrated TE airfoil

(c) Combed TE airfoil (d) Comb-Serrated TE airfoil

(e) Poro-Serrated TE airfoil

Fig. 12. Velocity Profile at α = 2^0

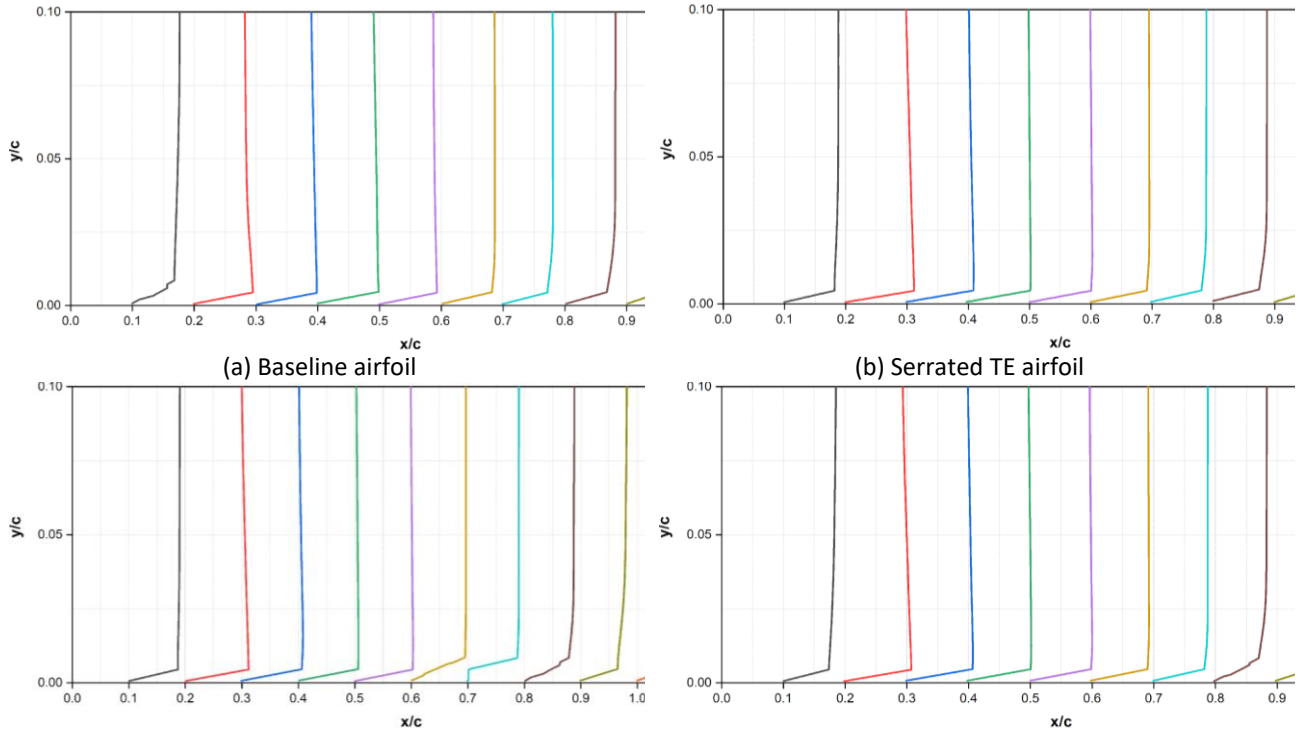

(a) Baseline airfoil (b) Serrated TE airfoil

(c) Combed TE airfoil (d) Comb-Serrated TE airfoil

Fig. 13. Velocity Profile at α = 3^0

Furthermore, the velocity profile graphs give insight into the flow characteristics of the combed and comb-serrated models. The combed model demonstrates a uniform flow from a zero angle of attack to 8 degrees. However, when the angle of attack increases from 8 to 10 degrees, a minor disruption in the flow along the trailing edge is seen. The flow separation is seen to occur at roughly 0.98c and 0.9c for angles of attack of 8 degrees and 10 degrees, respectively, resulting in a separation zone that is less than 10% of the chord length. The x-velocity contour shown in Figure 10 further verifies this observation. Similarly, the comb-serrated model reveals flow patterns comparable to the combed trailing-edge design. The flow through this model is shown to be laminar, starting from a zero angle of attack till 8 degrees. Even at high angles of attack of 10 degrees, the flow only separates along the trailing edge, resulting in a minimum separation part of less than 5% of the chord length. These findings show the potential of the comb-serrated model to sustain laminar flow over a vast range of angles of attack, resulting in a smaller separation zone as demonstrated earlier.

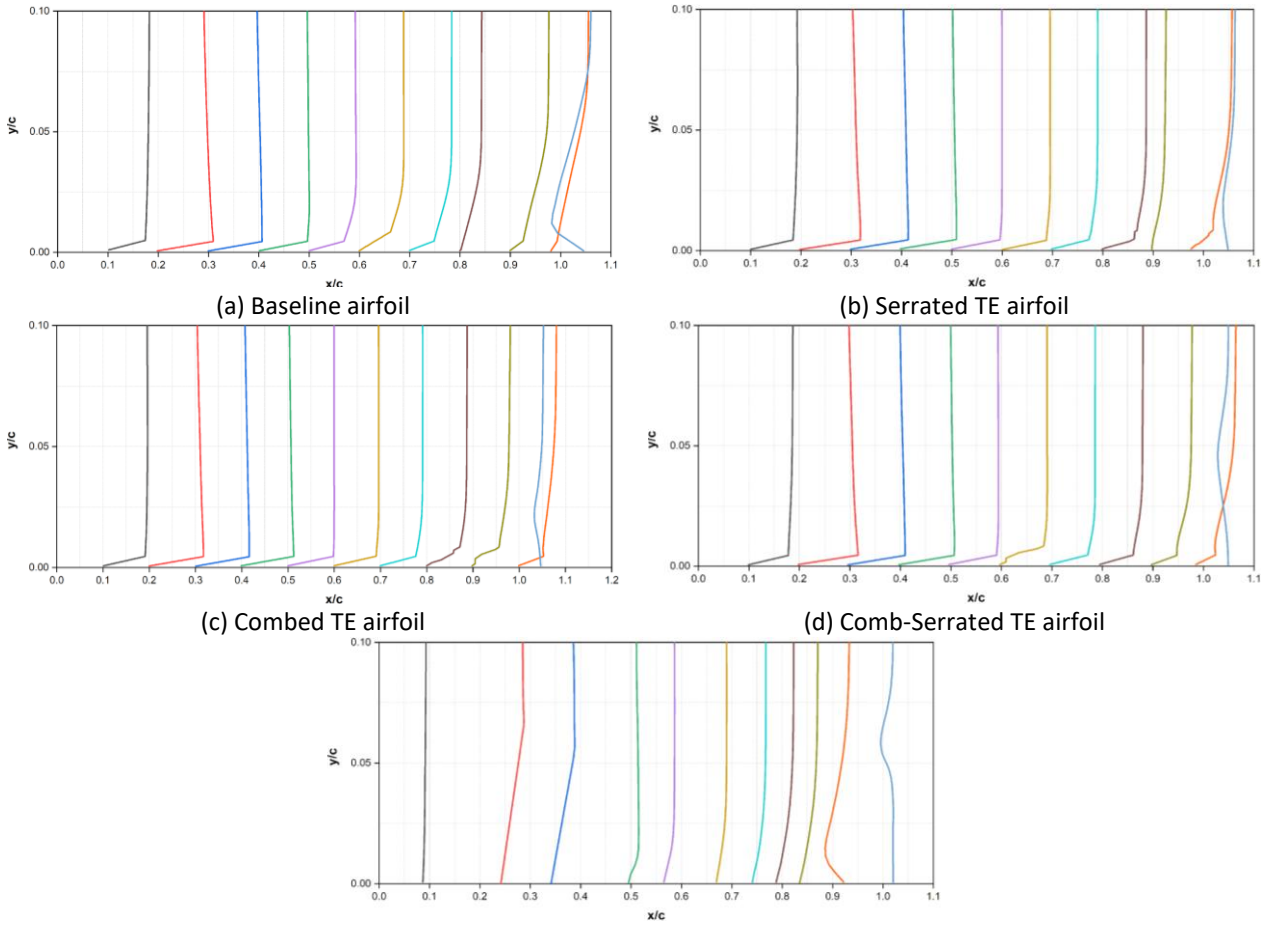

(a) Baseline airfoil

(b) Serrated TE airfoil

(c) Combed TE airfoil

(d) Comb-Serrated TE airfoil

(e) Poro-Serrated TE airfoil

Fig. 14. Velocity Profile at $\alpha = 6^0$

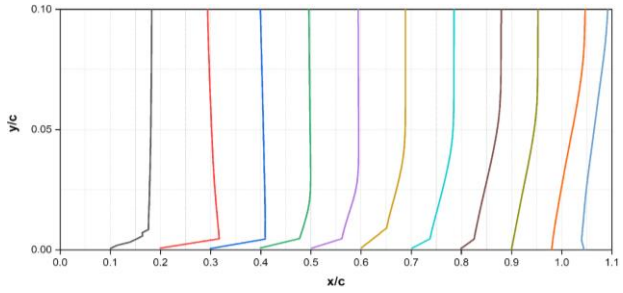

(a) Baseline airfoil

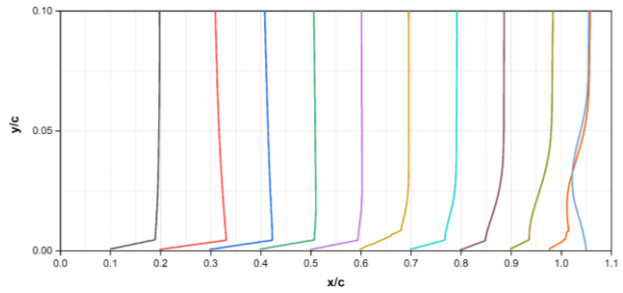

(b) Serrated TE airfoil

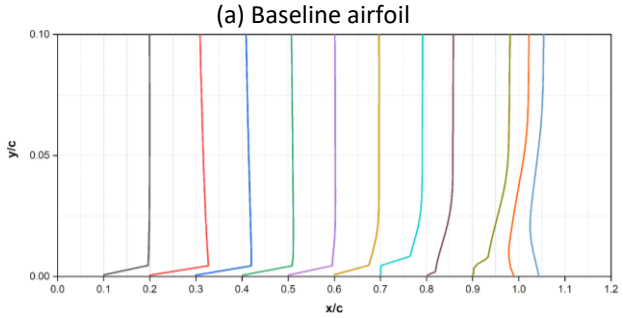

(c) Combed TE airfoil

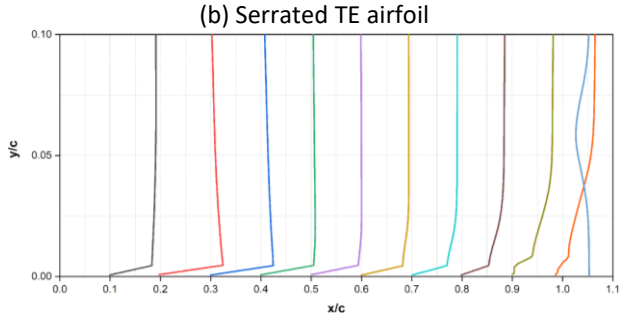

(d) Comb-Serrated TE airfoil

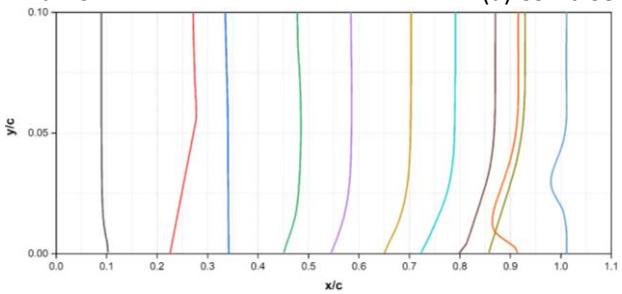

(e) Poro-Serrated TE airfoil

Fig. 15. Velocity Profile at $\alpha = 8^0$

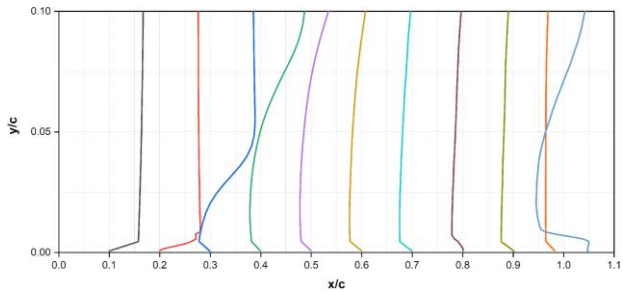

(a) Baseline airfoil

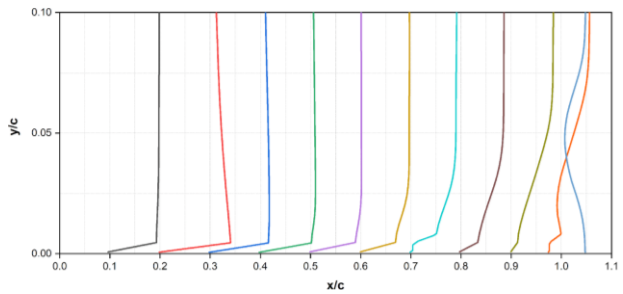

(b) Serrated TE airfoil

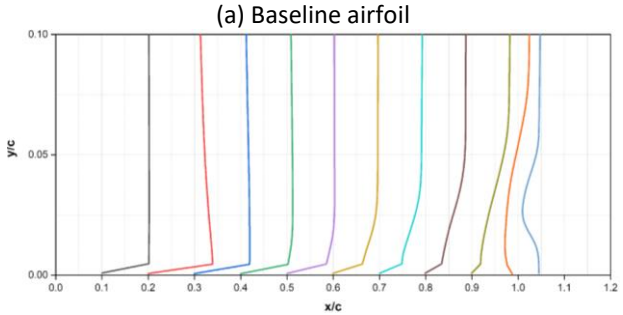

(c) Combed TE airfoil

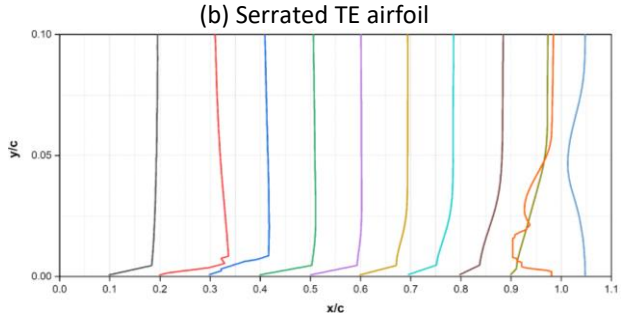

(d) Comb-Serrated TE airfoil

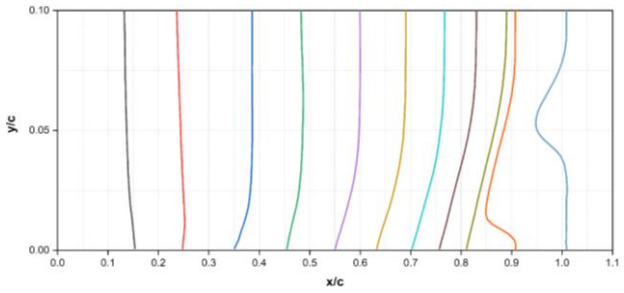

(e) Poro-Serrated TE airfoil

Fig. 16. Velocity Profile at α = 10^0

From the velocity profile graph, the poro-serrated model separates at around 0.6c at a zero angle of attack. This flow reattaches with the surface towards the trailing edge, forming a laminar separation bubble roughly 40% of the chord length. As the angle of attack is adjusted to 6, 8 and 10 degrees, the flow is found to separate at around 0.93c, 0.9c and 0.85c, respectively. This pattern demonstrates how the separation point shifts upstream as the angles of attack increase. Additionally, flow separation without reattachment is observed, thereby preventing the formation of a separation bubble. As a result, the poro-serrated model exhibits unique flow behaviors compared to other models, attributed to its capacity to allow air to pass through its porous region. These distinct separation patterns provide valuable insights into the effectiveness of the poro-serrated design in altering the flow dynamics over an airfoil surface.

4.3 Spanwise Vorticity

Figure 17 to Figure 22 contain specific information that helps to understand the three-dimensional flow structure visually and thoroughly. Vorticity defines the rotational movement of fluid elements within a fluid flow. To determine the velocity vector from PIV analysis, the displacement of tracer particles is evaluated across consecutive images and then divided by the time elapsed. The computation of the curl applied to these velocity vectors reveals vorticity vectors, indicating the local rotational motion of fluid elements. Represented usually as a vector, each component represents the rate of rotation around a specific axis. The spanwise vorticity plots for several models are provided and compared to clearly illustrate the causes for their discrepancies. At a zero angle of attack, the vorticity is seen to vary at the trailing edge with the exception at the root of the combed-type trailing edge. The poro-serrated model displays unsteadiness throughout the trailing edge, starting at 0.6c and extending until near the tip of the trailing edge. This finding reveals the rolling of the shear layers after separation, generating a recirculation zone that reattaches with the surface towards the tip of the trailing edge. The serration design also displays an unsteady zone near the trailing edge's end. As the angle of attack is raised from 0 to 2 degrees, the behaviour of the spanwise vorticity differs for different models. Generally, the spanwise vorticity behaviour at an angle of attack of 2 degrees is slightly similar with observations conducted at a zero angle of attack. The poro-serrated and serrated models displayed significant degrees of unsteadiness than other models. However, it was noticed that the unsteadiness in these models had substantially diminished as the angle of attack increased. This reduction in unsteadiness illustrates the sensitivity of the flow structures to changes in the angle of attack. In contrast, the other models indicated a slight increase in the spanwise vorticity. This rise, however, was relatively minimal. In particular, the poro-serrated model revealed a considerable shift in the flow patterns. The unsteadiness, previously found at the trailing edge, was noted to have shifted upstream. This variation in behaviour reveals its flow systems' complex and dynamic character. The comb model demonstrated a specific behaviour in the

spanwise vorticity as the angle of attack increased from 0 to 2 degrees. Unlike the serrated and poro-serrated models, which indicated the separation of the flow and formation of a bubble, the flow along the root of the comb model was shown to have shifted further away from the trailing edge.

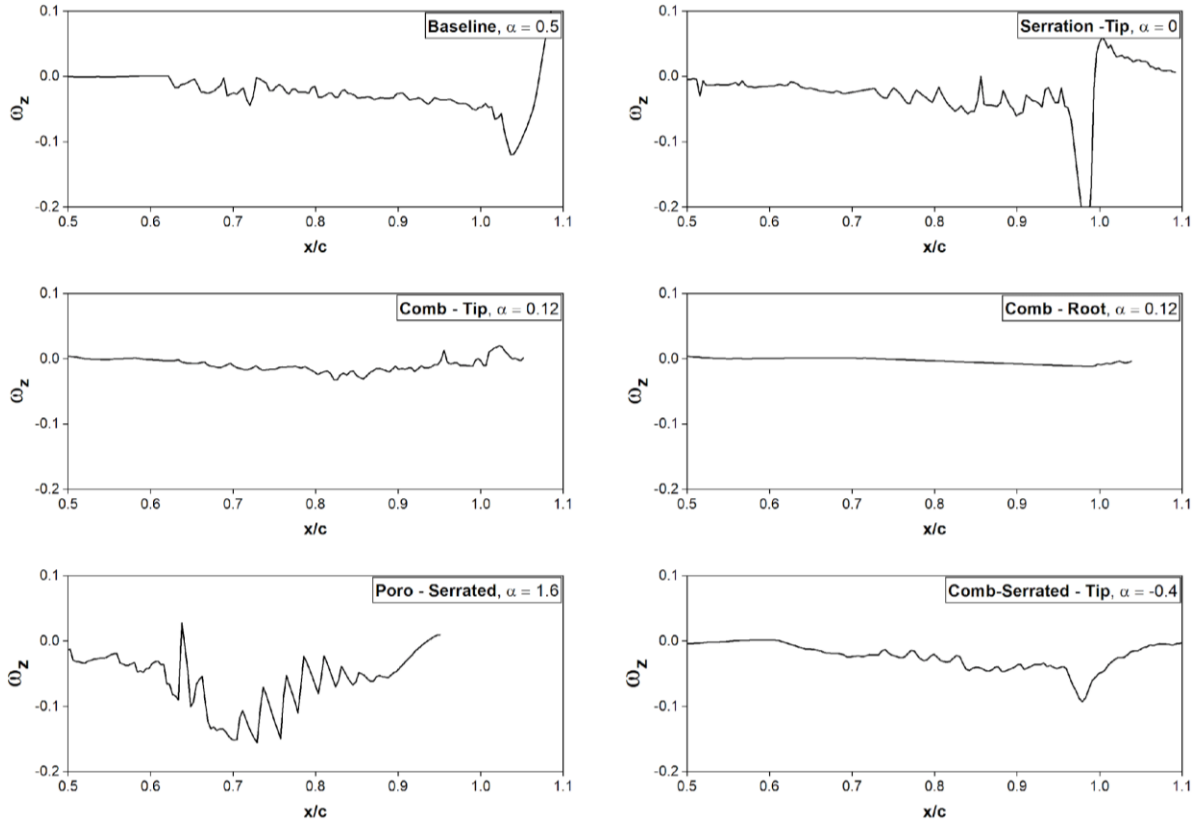

Fig. 17. Spanwise Vorticity at α = 0^0

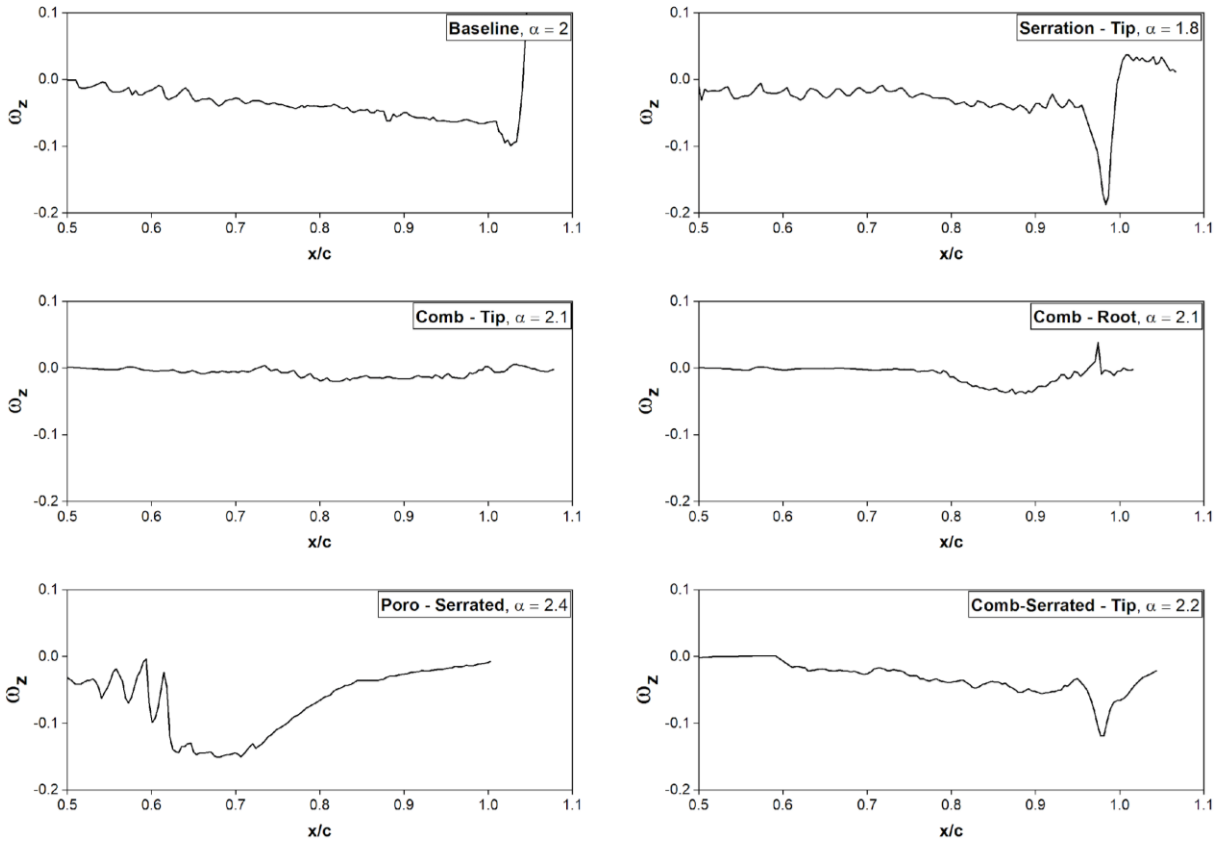

Fig. 18. Spanwise Vorticity at $\alpha = 2^0$

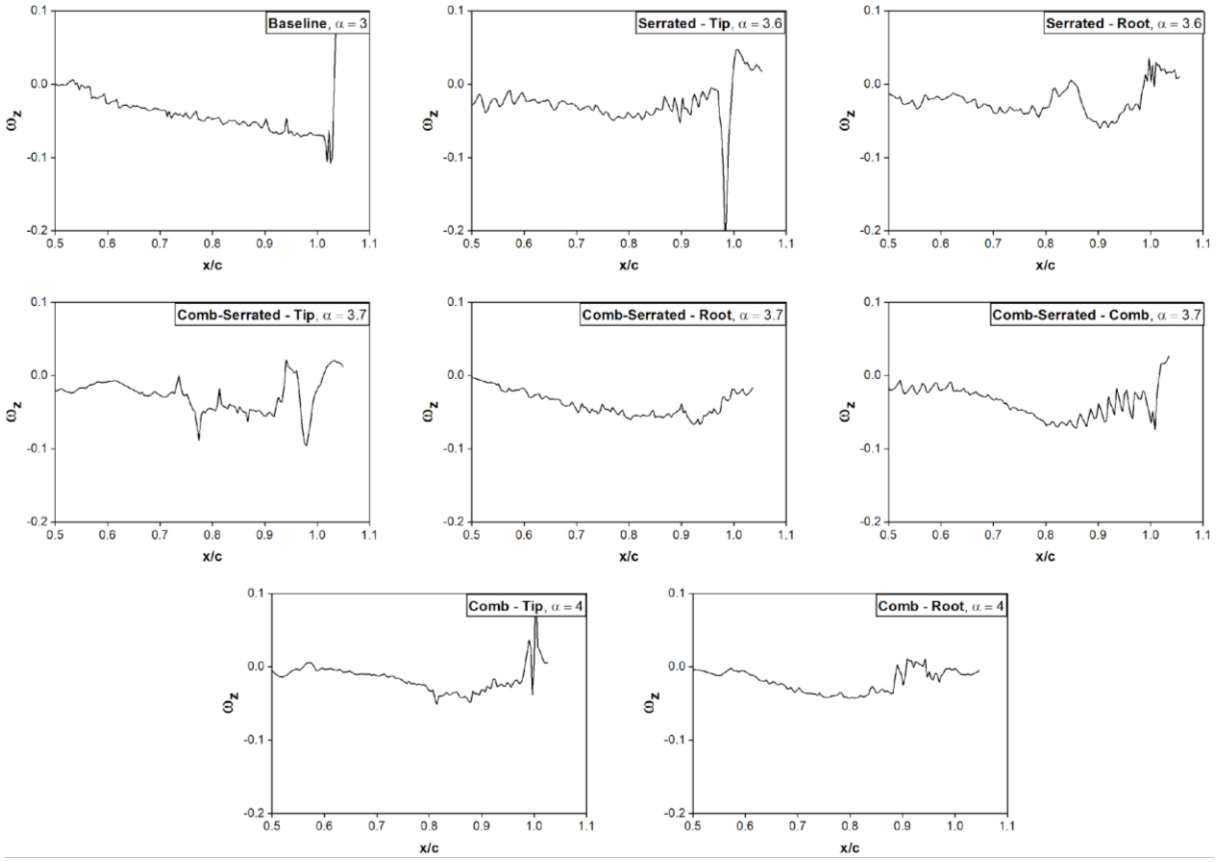

Fig. 19. Spanwise Vorticity at $\alpha = 3^0$

At an angle of attack of 3 degrees, the spanwise vorticity over the baseline model gradually increases compared to the results at 2 degrees. In the case of the serration design, the flow continues to demonstrate a rolling behaviour near the end of the trailing edge as it advances into the wake zone. At this angle of attack, the serration's root section displays a higher amount of unsteadiness than the tip component. The root section displays more significant oscillations in the spanwise vorticity as contrasted to the tip, which is observed to detach more swiftly. These findings imply that the flow is getting increasingly more unstable towards the root of the serration as the angle of attack increases from 2 to 3 degrees. Meanwhile, the comb design displays a pattern similar to the one observed at 2 degrees, with the flow moving away from the trailing edge and forming a more streamlined structure. The comb design continues to display a smooth flow over the surface without any evidence of separation. On another side, the spanwise vorticity values of the comb-serrated model reveal higher unsteadiness around the tip of the trailing edge than the other regions. The tip area displays the maximum level of unsteadiness, followed by the comb-like section, and the least amount of unsteadiness is detected along the root. These patterns show that the serration and comb configurations impact the flow in distinct ways, and the resulting spanwise vorticity values reflect these changes. Furthermore, as the angle of attack is increased from 3 to 6 degrees, a further rise in unsteadiness is noted in the spanwise vorticity of the baseline model. This rise is characterized by the development of a rolling structure and the growth of a laminar separation bubble as demonstrated by x-velocity contour. In the serrated model, the unsteadiness along the tip intensifies, with a decrease in the amplitude of the sudden disturbance noticed at the end of the trailing edge. The comb structure shows a sharp unsteadiness towards the tip of its geometry, comparable to the serration characteristic and ascribed to the bluntness of the trailing edge. However, the root component of the comb structure demonstrates less unsteadiness compared to the angle of attack of 3 degrees. In contrast, the poro-serrated model depicts a smooth flow with minor disruptions, which can be owing to the change in momentum from the airflow passing through the porous zone. Meanwhile, the comb-serrated model exhibits minimal variation compared to the angle of attack of 3 degrees, with more minor disruptions noted around the tip, root, and comb-like section of the trailing edge.

The results presented in Figure 20 and Figure 21 reveal that as the angle of attack is raised from 6 to 8 degrees, the spanwise vorticity in the baseline model undergoes a further upsurge in unsteadiness. This increase is evident by disturbances being monitored even in the wake region. The serration model likewise displays an increase in unsteadiness, with the root and tip sections experiencing more significant levels. Unlike the angle of attack of 6 degrees, the rapid disruption noted at the end of the trailing edge at the tip section is no longer present. Nonetheless, both the baseline and serration models demonstrate that the flow separates and reattaches near the end of the trailing edge, resulting in the development of a separation bubble. Similarly, the comb model demonstrates separation at the end of the trailing edge and forms separation bubbles at both the tip and root sections. The disturbance is more prominent near the end of the trailing edge in the root section, whereas the tip part sees a somewhat less disturbed flow. In contrast, the poro-serrated model displays a smooth flow with little perturbation. However, the flow is observed to detach, forming a tiny separation bubble after reattaching to the surface. On the other hand, the comb-serrated model demonstrates increasing disturbance levels along all sections. Unlike the root component, the tip and comb-like part reattach to the surface after separation. The root and comb segments generate larger amounts of unsteadiness in the flow than the other types. With the angle of attack of 10 degrees as shown in Figure 22, the flow across the baseline surface experiences a breakdown due to the excessive intensity of the nonlinear interaction. This phenomenon leads to the fast shedding of vortices downstream, clearly visible in Figure 22. However, the vortices are not

clearly apparent due to the high-pressure flow downstream. The spanwise vorticity of the serration model displays characteristics comparable to those found at an angle of attack of 8 degrees at the tip section. Despite this, the root section suffers a decrease in disturbance, marked by visible vortices. The comb model reveals patterns comparable to those found at an angle of attack of 8 degrees for both the tip and root sections. In contrast, the poro-serrated model demonstrates increased disturbance throughout the trailing edge surface, with separation visible throughout. Similarly, the comb-serrated model displays feature comparable to those seen at an angle of attack of 8 degrees, with a minor increase in unsteadiness along the root section.

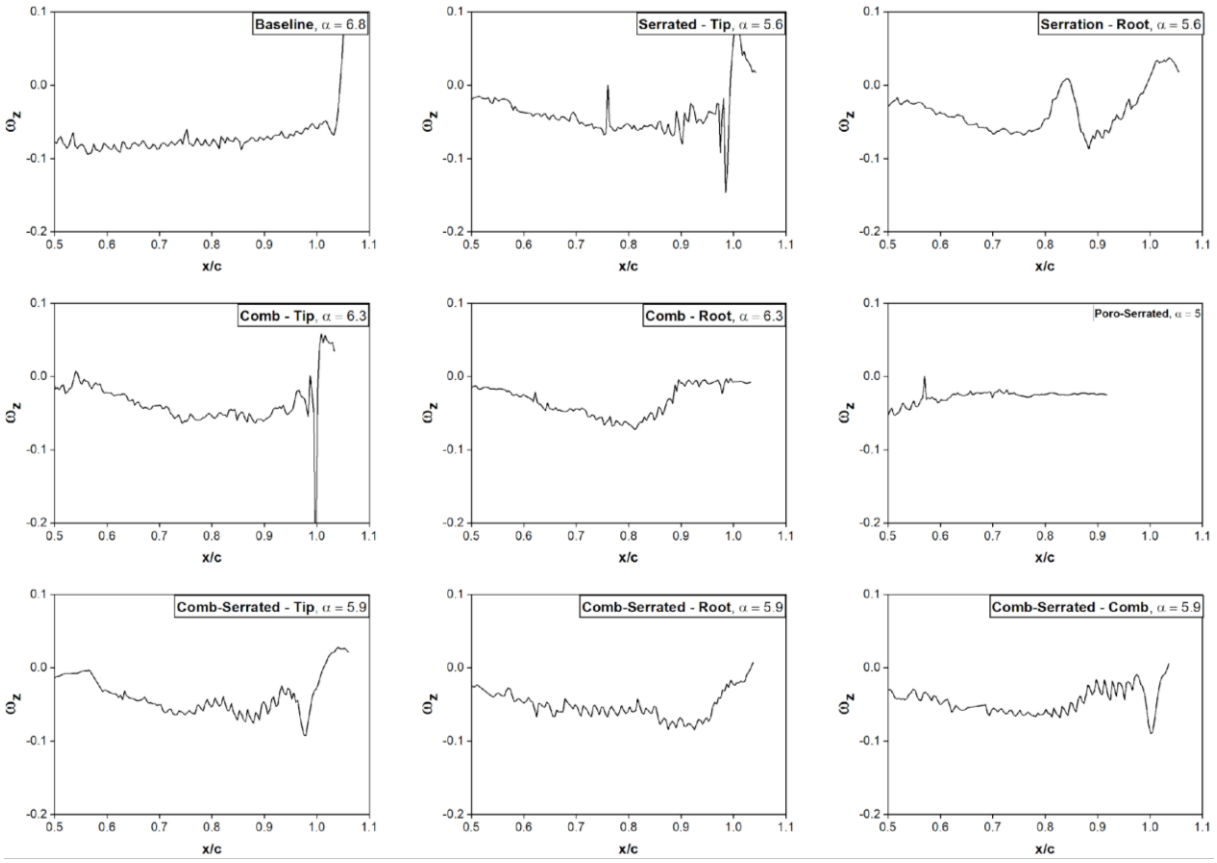

Fig. 20. Spanwise Vorticity at α = 6^0

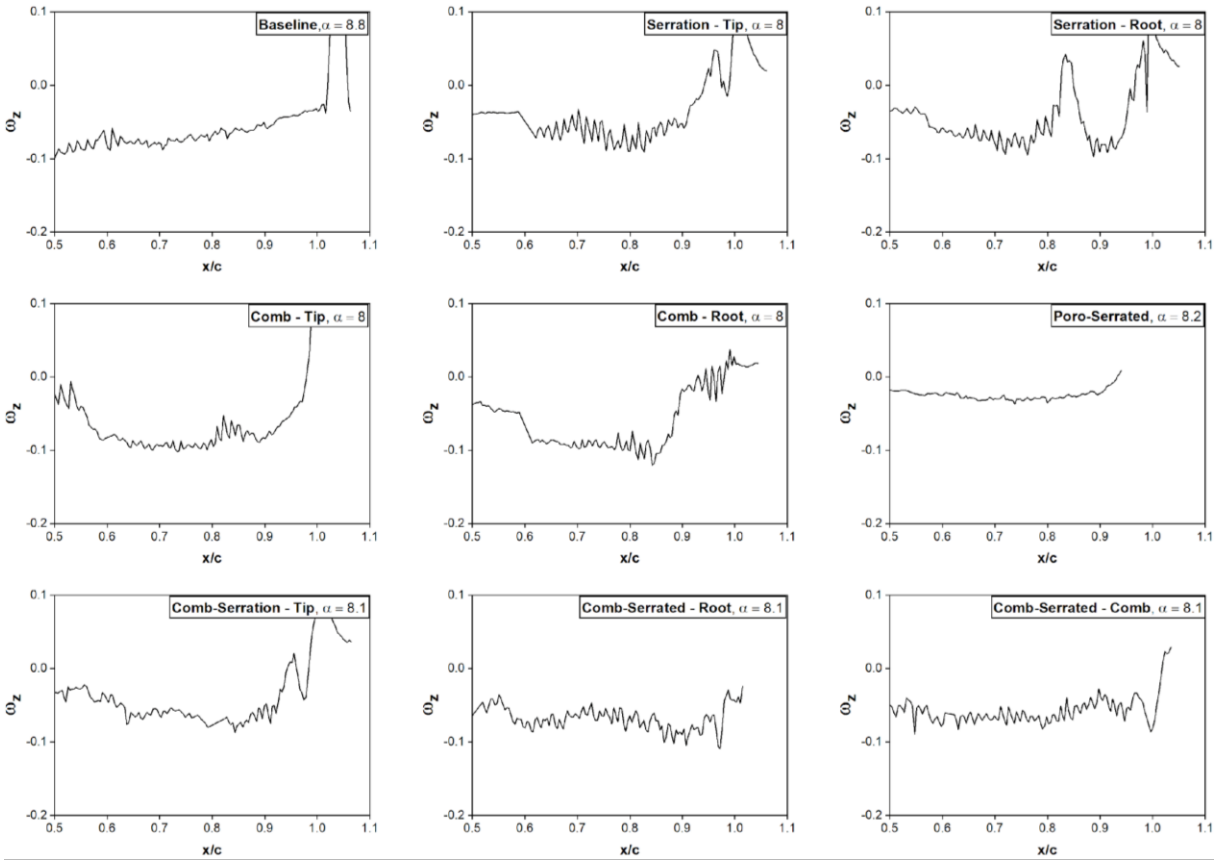

Fig. 21. Spanwise Vorticity at $\alpha = 8^0$

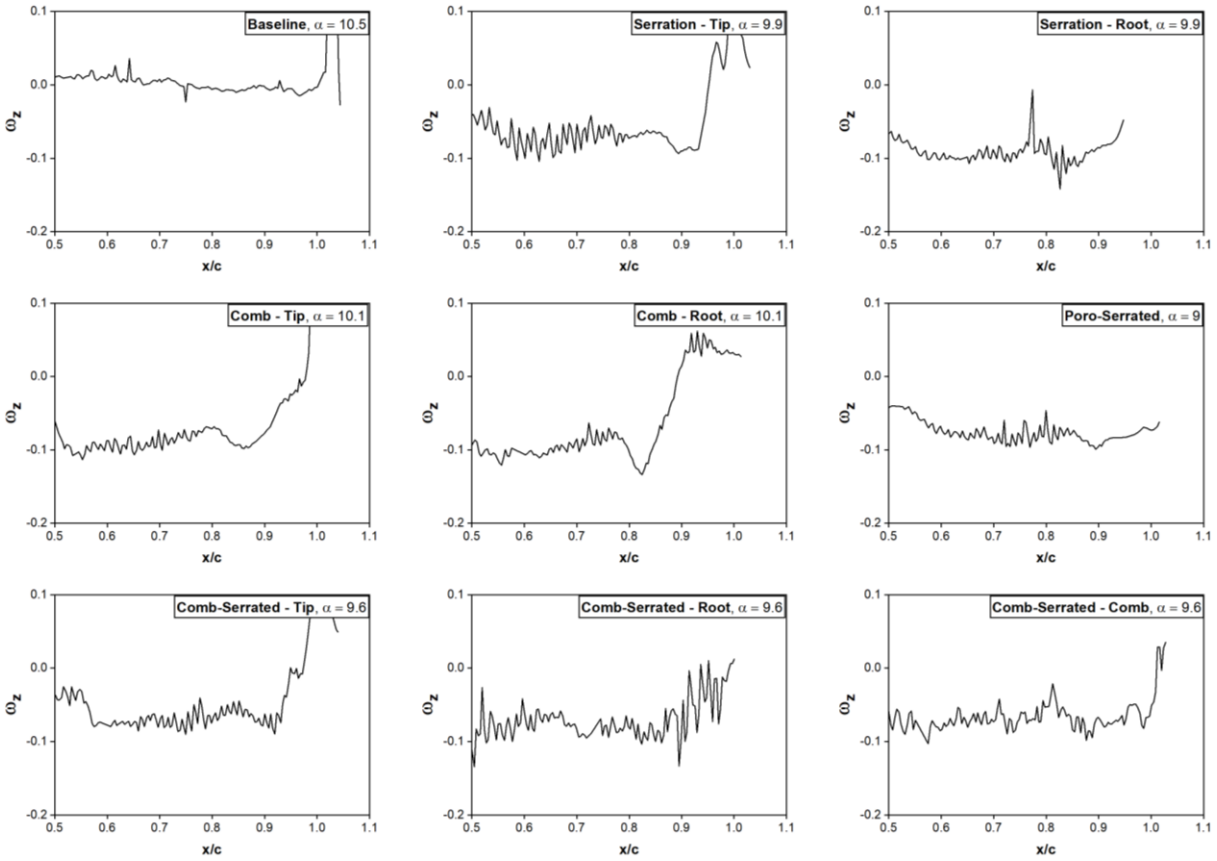

Fig. 22. Spanwise Vorticity at $\alpha = 10^0$

5. Conclusions

PIV experiments were conducted to gain a comprehensive understanding of the results, providing insights into the flow behavior of the aerodynamic system while highlighting areas for potential improvement in future design iterations. Through experimental investigations, the study reveals that Musou Black paint has a higher light absorption rate than flat black paint. Nevertheless, the latter exhibits a lower reflection level on a poro-serrated surface, indicating distinct differences between the two paints. The analysis of the x-velocity contour and spanwise vorticity analysis demonstrate that the serrated, combed, and comb-serrated airfoil models have more stable flow patterns and fewer separation bubbles compared to the baseline airfoil. This suggests a promising way of delaying flow separation, as these models consistently maintain stable flow patterns across various angles of attack. In contrast, the poro-serrated model displays a unique laminar separation bubble at zero angle of attack, possibly due to its porous surface disrupting the flow; however, this bubble disappears at a 2-degree angle of attack. The distinctive flow profile of the poro-serrated model warrants further exploration for its ability to delay flow separation, particularly at high angles of attack. Notably, at a 10-degree angle of attack, the serrated models confine separation regions to under 20% of the chord length, the comb model further reduces it to below 10%, and the comb-serrated design maintains laminar flow even at high angles of attack, with separation areas of less than 5%, compared to the baseline's 70% separation. Additionally, At 10 degrees angle of attack, the baseline model exhibits a breakdown of its shear layer, leading to disintegration, whereas the poro-serrated model showed increasing disturbance and separation. In contrast, the comb-serrated and serration models demonstrate a lesser increase in unsteadiness.

Acknowledgement

The research was supported by the Ministry of Education (MOE) through Fundamental Research Grant Scheme (FRGS/1/2018/TK09/UIAM/03/4). We would also like to thank IIUM for financial support under the KOE Postgraduate Tuition Fee Waiver Scheme 2019 (TFW2019).

References

[1] Ibren, Mohamed, Amelda Dianne Andan, Waqar Asrar, and Erwin Sulaeman. "A Review on Generation and Mitigation of Airfoil Self-Induced Noise." *Journal of Advanced Research in Fluid Mechanics and Thermal Sciences* 90, no. 1 (2022): 163-178. https://doi.org/10.37934/arfmts.90.1.163178

[2] Carmichael, B. H. *Low Reynolds number airfoil survey, volume 1*. No. NASA-CR-165803-VOL-1. 1981.

[3] Alam, Muhammad, and Neil D. Sandham. "Direct numerical simulation of 'short'laminar separation bubbles with turbulent reattachment." *Journal of Fluid Mechanics* 410 (2000): 1-28. https://doi.org/10.1017/S0022112099008976

[4] Counsil, Joshua NN, and Kiari Goni Boulama. "Low-reynolds-number aerodynamic performances of the NACA 0012 and Selig-Donovan 7003 Airfoils." *Journal of Aircraft* 50, no. 1 (2013): 204-216. https://doi.org/10.2514/1.C031856

[5] Malkiel, E., and R. E. Mayle. "Transition in a separation bubble." *Journal of Turbomachinery* 118, no. 4 (1996): 752-759. https://doi.org/10.1115/1.2840931

[6] Ibren, Mohamed, Amelda Dianne Andan, Waqar Asrar, and Erwin Sulaeman. "Laminar Separation Bubble and Flow Topology of NACA 0015 at Low Reynolds Number." *CFD Letters* 13, no. 10 (2021): 36-51. https://doi.org/10.37934/cfdl.13.10.3651

[7] Crivellini, Andrea, Valerio D'Alessandro, Daniele Di Benedetto, Sergio Montelpare, and Renato Ricci. "Study of laminar separation bubble on low Reynolds number operating airfoils: RANS modelling by means of an high-accuracy solver and experimental verification." In *Journal of Physics: Conference Series*, vol. 501, no. 1, p. 012024. IOP Publishing, 2014. https://doi.org/10.1088/1742-6596/501/1/012024

[8] Owen, P. R., and L. Klanfer. "On the laminar boundary layer separation from the leading edge of a thin aerofoil." *Aeronautical Reseach Council (ARC) CP* 220 (1955).

[9] Yuan, W., H. Xu, M. Khalid, and R. Radespiel. "A parametric study of LES on laminar-turbulent transitional flows past an airfoil." *International Journal of Computational Fluid Dynamics* 20, no. 1 (2006): 45-54. https://doi.org/10.1080/10618560600578492
[10] Kurelek, John W., Burak A. Tuna, Serhiy Yarusevych, and Marios Kotsonis. "Three-dimensional development of coherent structures in a two-dimensional laminar separation bubble." *AIAA Journal* 59, no. 2 (2021): 493-505. https://doi.org/10.2514/1.J059700
[11] Lei, Juanmian, Feng Guo, and Can Huang. "Numerical study of separation on the trailing edge of a symmetrical airfoil at a low Reynolds number." *Chinese Journal of Aeronautics* 26, no. 4 (2013): 918-925. https://doi.org/10.1016/j.cja.2013.06.005
[12] Kim, Dong-Ha, and Jo-Won Chang. "Low-Reynolds-number effect on the aerodynamic characteristics of a pitching NACA0012 airfoil." *Aerospace Science and Technology* 32, no. 1 (2014): 162-168. https://doi.org/10.1016/j.ast.2013.08.018
[13] Plogmann, B., A. Herrig, and W. Würz. "Experimental investigations of a trailing edge noise feedback mechanism on a NACA 0012 airfoil." *Experiments in Fluids* 54, no. 5 (2013): 1480. https://doi.org/10.1007/s00348-013-1480-z
[14] Goni Boulama, Kiari, and Joshua Counsil. "Validation of a low-cost transitional turbulence model for low-Reynolds-number external aerodynamics." In *20th AIAA Computational Fluid Dynamics Conference*, p. 3698. 2011. https://doi.org/10.2514/6.2011-3698
[15] Ma, Dongli, Yanping Zhao, Yuhang Qiao, and Guanxiong Li. "Effects of relative thickness on aerodynamic characteristics of airfoil at a low Reynolds number." *Chinese Journal of Aeronautics* 28, no. 4 (2015): 1003-1015. https://doi.org/10.1016/j.cja.2015.05.012
[16] Chen, Nanshu, Hanru Liu, Qian Liu, Xingyu Zhao, and Yangang Wang. "Effects and mechanisms of LES and DDES method on airfoil self-noise prediction at low to moderate Reynolds numbers." *AIP Advances* 11, no. 2 (2021). https://doi.org/10.1063/5.0038183
[17] Selig, Michael, James Guglielmo, Andy Broern, and Philippe Giguere. "Experiments on airfoils at low Reynolds numbers." In *34th Aerospace Sciences Meeting and Exhibit*, p. 62. 1996. https://doi.org/10.2514/6.1996-62
[18] Lissaman, P. B. S. "Low-Reynolds-number airfoils." *Annual Review of Fluid Mechanics* 15, no. 1 (1983): 223-239. https://doi.org/10.1146/annurev.fl.15.010183.001255
[19] Dassen, T., R. Parchen, J. Bruggeman, and F. Hagg. "Results of a wind tunnel study on the reduction of airfoil self-noise by the application of serrated blade trailing edges." In *1996 European Union Wind Energy Conference and Exhibition*, Gothenburg, 20-24 May, pp. 8. 1996.
[20] Oerlemans, S., J. G. Schepers, G. Guidati, and S. Wagner. "Experimental demonstration of wind turbine noise reduction through optimized airfoil shape and trailing-edge serrations." In *Proceedings of the European Wind Energy Conference and Exhibition*, Copenhagen, 2-6 July. 2001.
[21] Gruber, Mathieu, Phil Joseph, and Tze Pei Chong. "Experimental investigation of airfoil self noise and turbulent wake reduction by the use of trailing edge serrations." In *16th AIAA/CEAS Aeroacoustics Conference*, p. 3803. 2010. https://doi.org/10.2514/6.2010-3803
[22] Chong, Tze Pei, and Phillip F. Joseph. "An experimental study of airfoil instability tonal noise with trailing edge serrations." *Journal of Sound and Vibration* 332, no. 24 (2013): 6335-6358. https://doi.org/10.1016/j.jsv.2013.06.033
[23] Moreau, Danielle J., Laura A. Brooks, and Con J. Doolan. "Flat plate self-noise reduction at low-to-moderate Reynolds number with trailing edge serrations." In *Proceedings of ACOUSTICS*, pp. 2-4. 2011.
[24] Jones, Lloyd, and Richard Sandberg. "Numerical investigation of airfoil self-noise reduction by addition of trailing-edge serrations." In *16th AIAA/CEAS Aeroacoustics Conference*, p. 3703. 2010. https://doi.org/10.2514/6.2010-3703
[25] Sandberg, R. D., and L. E. Jones. "Direct numerical simulations of low Reynolds number flow over airfoils with trailing-edge serrations." *Journal of Sound and Vibration* 330, no. 16 (2011): 3818-3831. https://doi.org/10.1016/j.jsv.2011.02.005
[26] Chong, T. P., P. F. Joseph, and M. Gruber. "Airfoil self noise reduction by non-flat plate type trailing edge serrations." *Applied Acoustics* 74, no. 4 (2013): 607-613. https://doi.org/10.1016/j.apacoust.2012.11.003
[27] Howe, Michael S. "Noise produced by a sawtooth trailing edge." *The Journal of the Acoustical Society of America* 90, no. 1 (1991): 482-487. https://doi.org/10.1121/1.401273
[28] Lyu, Benshuai, Mahdi Azarpeyvand, and Samuel Sinayoko. "Prediction of noise from serrated trailing edges." *Journal of Fluid Mechanics* 793 (2016): 556-588. https://doi.org/10.1017/jfm.2016.132
[29] Chong, Tze Pei, and Alexandros Vathylakis. "On the aeroacoustic and flow structures developed on a flat plate with a serrated sawtooth trailing edge." *Journal of Sound and Vibration* 354 (2015): 65-90. https://doi.org/10.1016/j.jsv.2015.05.019

[30] Lau, Alex SH, Sina Haeri, and Jae Wook Kim. "The effect of wavy leading edges on aerofoil-gust interaction noise." *Journal of Sound and Vibration* 332, no. 24 (2013): 6234-6253. https://doi.org/10.1016/j.jsv.2013.06.031
[31] Lyu, Benshuai, and Mahdi Azarpeyvand. "On the noise prediction for serrated leading edges." *Journal of Fluid Mechanics* 826 (2017): 205-234. https://doi.org/10.1017/jfm.2017.429
[32] Vathylakis, Alexandros, Tze Pei Chong, and Phillip F. Joseph. "Poro-serrated trailing-edge devices for airfoil self-noise reduction." *AIAA Journal* 53, no. 11 (2015): 3379-3394. https://doi.org/10.2514/1.J053983
[33] Sueki, Takeshi, Takehisa Takaishi, Mitsuru Ikeda, and Norio Arai. "Application of porous material to reduce aerodynamic sound from bluff bodies." *Fluid Dynamics Research* 42, no. 1 (2010): 015004. https://doi.org/10.1088/0169-5983/42/1/015004
[34] Liu, Hanru, Jinjia Wei, and Zhiguo Qu. "Prediction of aerodynamic noise reduction by using open-cell metal foam." *Journal of Sound and Vibration* 331, no. 7 (2012): 1483-1497. https://doi.org/10.1016/j.jsv.2011.11.016
[35] Herr, Michaela, Karl-Stephane Rossignol, Jan Delfs, Nicolas Lippitz, and Michael Mößner. "Specification of porous materials for low-noise trailing-edge applications." In *20th AIAA/CEAS Aeroacoustics Conference*, p. 3041. 2014. https://doi.org/10.2514/6.2014-3041
[36] Geyer, Thomas. "Trailing edge noise generation of porous airfoils." PhD diss., BTU Cottbus-Senftenberg, 2011.
[37] Lissaman, P. B. S. "Low-Reynolds-number airfoils." *Annual Review of Fluid Mechanics* 15, no. 1 (1983): 223-239. https://doi.org/10.1146/annurev.fl.15.010183.001255
[38] Koh, Seong Ryong, Beckett Zhou, Matthias Meinke, Nicolas Gauger, and Wolfgang Schröder. "Numerical analysis of the impact of variable porosity on trailing-edge noise." *Computers & Fluids* 167 (2018): 66-81. https://doi.org/10.1016/j.compfluid.2018.02.015
[39] Carpio, Alejandro Rubio, Roberto Merino Martínez, Francesco Avallone, Daniele Ragni, Mirjam Snellen, and Sybrand van der Zwaag. "Experimental characterization of the turbulent boundary layer over a porous trailing edge for noise abatement." *Journal of Sound and Vibration* 443 (2019): 537-558. https://doi.org/10.1016/j.jsv.2018.12.010
[40] Bernicke, Paul, R. A. D. Akkermans, Varun B. Ananthan, Roland Ewert, Jürgen Dierke, and Lennart Rossian. "A zonal noise prediction method for trailing-edge noise with a porous model." *International Journal of Heat and Fluid Flow* 80 (2019): 108469. https://doi.org/10.1016/j.ijheatfluidflow.2019.108469
[41] Herr, Michaela, and Johann Reichenberger. "In search of airworthy trailing-edge noise reduction means." In *17th AIAA/CEAS Aeroacoustics Conference (32nd AIAA Aeroacoustics Conference)*, p. 2780. 2011. https://doi.org/10.2514/6.2011-2780
[42] Zhang, Minghui, and Tze Pei Chong. "Experimental investigation of the impact of porous parameters on trailing-edge noise." *Journal of Sound and Vibration* 489 (2020): 115694. https://doi.org/10.1016/j.jsv.2020.115694
[43] Revell, James, James Revell, Herbert Kuntz, Frank Balena, Clifton Horne, Bruce Storms, Robert Dougherty et al. "Trailing-edge flap noise reduction by porous acoustic treatment." In *3rd AIAA/CEAS Aeroacoustics Conference*, p. 1646. 1997. https://doi.org/10.2514/6.1997-1646
[44] Bernstein, Leonard. "Force measurements in short-duration hypersonic facilities." *Neuilly-sur-Seine, France: AGARD*, 1975.
[45] Hilton, W. F. "Low Speed Wind Tunnel Testing. Alan Pope and John J. Harper and John J. Harper. John Wiley & Sons, New York. 1966. 457pp. Illustrations. Diagrams. Tables. 110s." *The Aeronautical Journal* 71, no. 678 (1967): 445-445. https://doi.org/10.1017/S000192400005569X
[46] Musou Black. "The Blackest Shop in Europe!." *Musou Black*. Accessed December 6, 2023. https://www.musoublack.com/.